Bose-Einstein condensation in systems with flux equilibrium

Victor S. L'vov, Anna Pomyalov, Sergey V. Nazarenko, Dmytro A. Bozhko, Alexander J. E. Kreil, Burkard Hillebrands, and Alexander A. Serga

Phys. Rev. B **109**, 014301 — Published 3 January 2024

DOI: 10.1103/PhysRevB.109.014301

Bose-Einstein condensation in systems with flux equilibrium

Victor S. L'vov,[1,*] Anna Pomyalov,[2,†] Sergey V. Nazarenko,[3,‡] Dmytro A. Bozhko,[4,§]
Alexander J. E. Kreil,[5,¶] Burkard Hillebrands,[5,**] and Alexander A. Serga[5,††]

[1] *Department of Physics of Complex Systems, Weizmann Institute of Science, Rehovot 76100, Israel*
[2] *Department of Chemical and Biological Physics, Weizmann Institute of Science, Rehovot 76100, Israel*
[3] *Université Côte d'Azur, CNRS, Institut de Physique de Nice, 17 rue Julien Lauprêtre 06200 Nice, France*
[4] *Department of Physics and Energy Science, University of Colorado Colorado Springs, Colorado Springs, Colorado 80918, USA*
[5] *Fachbereich Physik and Landesforschungszentrum OPTIMAS, Rheinland-Pfälzische Technische Universität Kaiserslautern-Landau, 67663 Kaiserslautern, Germany*

We consider flux equilibrium in dissipative nonlinear wave systems subject to external energy pumping. In such systems, the elementary excitations, or quasiparticles, can create a Bose-Einstein condensate. We develop a theory on the Bose-Einstein condensation of quasiparticles for various regimes of external excitation, ranging from weak and stationary to ultra-strong pumping, enabling us to determine the number of quasiparticles near the bottom of the energy spectrum and their distribution along wave vectors. We identify physical phenomena leading to condensation in each of the regimes. For weak stationary pumping, where the distribution of quasiparticles deviates only slightly from thermodynamic equilibrium, we define a range of pumping parameters where the condensation occurs and estimate the density of the condensate and the fraction of the condensed quasiparticles. As the pumping amplitude increases, a powerful influx of injected quasiparticles is created by the Kolmogorov-Zakharov scattering cascade, leading to their Bose-Einstein condensation. With even stronger pumping, kinetic instability may occur, resulting in a direct transfer of injected quasiparticles to the bottom of the spectrum. For the case of ultra-strong parametric pumping, we have developed a stationary nonlinear theory of kinetic instability. The theory agrees qualitatively with experimental data obtained using Brillouin light scattering spectroscopy during parametric pumping of magnons in room-temperature films of yttrium-iron garnet.

I. INTRODUCTION

The Bose-Einstein (BE) condensate (BEC) is a state of matter with a macroscopically large number of bosons occupying the lowest quantum state and demonstrating coherence at macroscopic scales [1–5]. This phenomenon was observed and investigated in atomic systems such as ^{4}He, ^{3}He (in the latter, the role of bosons is played by Cooper pairs of fermionic ^{3}He atoms), and in ultra-cold trapped atoms [6, 7].

BECs were also found in systems of bosonic quasiparticles such as polaritons [8] and excitons [9] in semiconductors, photons in micro-cavities [10], as well as magnons in superfluid ^{3}He [11] and magnetic crystalline materials [12–14]. In all these cases quasiparticles have a finite lifetime, and the appearance of steady-state BEC requires continuous or periodic excitation (pumping) of quasiparticles by an external source. To some extent, these systems can be considered as being in a flux-defined (rather than thermodynamic) equilibrium. This feature makes the quasiparticle systems qualitatively different from the systems of real particles (atoms) whose total number is conserved. BECs of quasiparticles are drawing significant interest for their possible applications in new technologies of information transfer and data processing, including coherent quantum optics (see, e.g., [15–17]). The investigation of such flux-driven systems is the main motivation of the present work.

In this paper, we compare various scenarios of the evolution of a weakly interacting overpopulated gas of quasiparticles toward BEC under conditions of flux equilibrium. For simplicity, we consider an isotropic homogeneous wave system with a parabolic dispersion law:

$$\omega_k = \omega_0[1 + (ak)^2] \,. \tag{1a}$$

Here ω_0 is the gap of the frequency spectrum ("bottom" frequency), a is a characteristic scale, and k is the wave number, see Fig. 1. This choice simplifies the comparison of a BEC of quasiparticles with the energy $E_k = \hbar\omega_k$ in the flux-equilibrium wave systems with a BEC of nonrelativistic bosons with the energy

$$E_k = (\hbar k)^2/(2m) \tag{1b}$$

expressed via the Plank's constant $h = 2\pi\hbar$ and the particle mass m. Expressions for E_k stress the wave-particle duality in describing waves and quasiparticles in quantum mechanics. For example, using the parabolic dispersion law (1a), we write an equation for energy similar to Eq. (1b),

$$E_k = E_0 + (\hbar k)^2/(2m)\,, \quad E_0 \equiv \hbar\omega_0 \,. \tag{1c}$$

* victor.lvov@gmail.com
† anna.pomyalov@weizmann.ac.il
‡ sergey.nazarenko@unice.fr
§ dbozhko@uccs.edu
¶ ajek91+tuk@gmail.com
** hilleb@rptu.de
†† serha@rptu.de

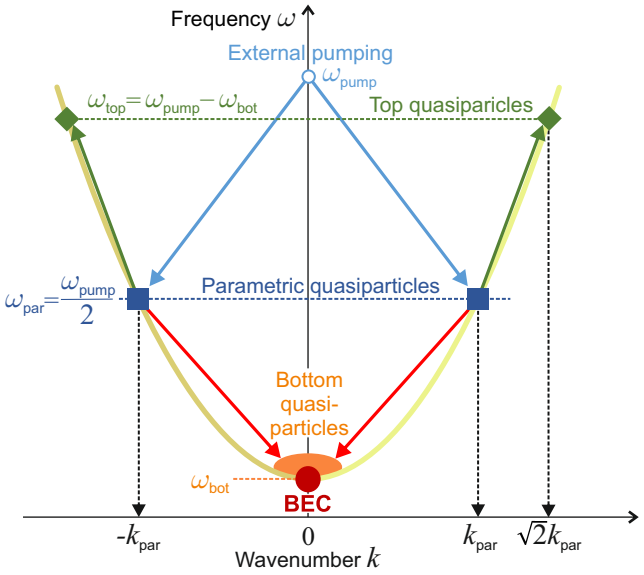

FIG. 1. Schematic representation of the parabolic frequency spectra of quasiparticles (1a) with their relevant groups: parametric quasiparticles with frequency $\omega_{\rm par}$, denoted as blue squares ■, BEC with frequency ω_0, denoted as red circles ●, and top quasiparticles with the frequency $\omega_{\rm top} = 2\omega_{\rm par} - \omega_{\rm bot}$, denoted as green diamonds ♦. The bottom quasiparticles slightly above the frequency $\omega_{\rm bot}$ are shown by the orange area. The light-blue arrows denote the process of creation of parametric quasiparticles by external pumping. The red and green arrows show the process of four-wave scattering, leading to the phenomenon of kinetic instability.

Thus, we can consider quasiparticles having the energy spectrum $E_k = \hbar\omega_k$ with ω_k defined by Eq. (1a) and an effective mass

$$m_{\rm eff} = \hbar/(2\omega_0 a^2)\ . \tag{1d}$$

To simplify the discussion further we assume that the pumping of the system results in the appearance of quasiparticles with a particular frequency $\omega_{\rm par}$. A well-known example of such pumping is the parametric excitation of magnons in a ferromagnetic material by an almost homogeneous external electromagnetic field of frequency $\omega_{\rm pump} = 2\omega_{\rm par}$. In this case, parametric magnons with frequency $\omega_{\rm par} = \omega(\pm\boldsymbol{k}_{\rm par})$ appear as a result of the decay process with the conservation law:

$$\omega_{\rm pump} = \omega(\boldsymbol{k}_{\rm par}) + \omega(-\boldsymbol{k}_{\rm par})\,, \tag{2}$$

schematically shown by two blue arrows in Fig. 1. All our results can be easily generalized for more sophisticated quasiparticle pumping in a wide range of frequencies, for example by parametric pumping with a noisy electromagnetic field (or noise modulation of quasiparticle frequency) [18].

The paper aims to investigate the processes leading to the emergence of Bose-Einstein condensates (BECs) in various parameter ranges of the pumping. It also seeks to determine the total number of quasiparticles ($N_{\rm tot}$) in the vicinity of the spectral minimum ω_0 and the fraction $N_{\rm BEC}$ of the number of quasiparticles that constitute the condensed part.

The structure of the paper is as follows. In Sec. II we describe the wave system under consideration and, to introduce notations, remind the well-known results for BE condensation of bosons in three-dimensional (3D) and two-dimensional (2D) systems.

Next, in Sec. III we formulate criteria for the BE condensation and find $N_{\rm tot}$ and $N_{\rm BE}$ for a relatively simple case of weak pumping, for which the nonlinear wave system, even in the presence of the energy and particle number fluxes, is close to the thermodynamic equilibrium. In Sec. IV we consider the case of strong pumping. Here, in the 3D system, the overpopulated gas of quasiparticles is transferred by step-by-step cascade processes down the frequency band, followed by the thermalization of low-energy quasiparticles into the BEC state [19, 20]. We also discuss more involved 2D and thin-film cases.

A very strong pumping regime, as considered in Sec. V, to the best of our knowledge, is currently realized only for magnons in ferromagnetic materials. However, the physical picture in this regime does not depend on the specific properties of magnons. We, therefore, consider quasiparticles with a generic parabolic frequency spectrum, shown in Fig. 1. Here, the cascade process can be accompanied by a direct transfer of the parametrically injected quasiparticles to the lowest (bottom) and high (top) energy states by a $2 \Leftrightarrow 2$ scattering process [21–23]

$$\omega(\boldsymbol{k}_{\rm par}) + \omega(\boldsymbol{k}'_{\rm par}) \Rightarrow \omega(\boldsymbol{k}_{\rm bot}) + \omega(\boldsymbol{k}_{\rm top})\ . \tag{3}$$

In this process, referred to as the kinetic instability (KI) [21], a dense cloud of incoherent "bottom" quasiparticles is formed close to the BEC point. This scattering process is sketched in Fig. 1 by red arrows pointing from blue-filled squares to the orange area and discussed in Sec. V A. By the energy conservation law (3), the same number of parametric quasiparticles is transferred to higher energy states with frequency $\omega_{\rm top} \simeq 2\omega_{\rm p} - \omega_{\rm b}$ and energy above thermodynamic equilibrium (top quasiparticles, shown in Fig. 1 by filled green diamonds). The feedback influence of the top and bottom quasiparticles on the parametric ones is studied in Sec. V B. Note that in the considered case of the parabolic isotropic dispersion surface, the momentum conservation law is satisfied because the parametric quasiparticles fill the entire isofrequency circle $\omega_{\rm par}$. Thus, the scattering process involves parametric quasiparticles with wave vectors $k_{\rm par}$ arranged at an angle of 45° to each other, which ensures that the wave vector length of the top quasiparticles is $\sqrt{2}k_{\rm par}$ (see Fig. 1). Four-particle scattering of parametric and bottom quasiparticles is responsible for the widening of the package of the bottom quasiparticles. These processes are considered in the framework of the nonlinear theory of kinetic instability, developed in Secs. V C and V D.

Section VI is devoted to the experimental study of the BE condensation of magnons in thin films of yttrium

iron garnet (YIG, $Y_3Fe_5O_{12}$) using Brillouin light scattering (BLS) spectroscopy. This ferrimagnetic material is a classical material for the experimental study of nonlinear magnon dynamics. There are several reasons for this: (i) most importantly, it has the lowest known spin-wave damping; (ii) its Curie temperature $T_C = 560\,\mathrm{K}$ allows experiments to be carried out at room temperature; (iii) being a dielectric, it is transparent to microwave electromagnetic radiation, which makes it possible to excite magnetic oscillations in the entire volume of bulk samples and study them using common microwave techniques; (iv) thin single-crystal films of YIG are transparent to visible light, which enables the study of magnon dynamics also by optical methods with spatial, temporal, frequency, and wave vector resolution. In our experiments, magnons were pumped by an external electromagnetic field, as shown in Fig. 8. Comparing the nonlinear theory of kinetic instability with available and new experimental results, we conclude that at large pumping amplitudes, kinetic instability is the main channel for transferring magnons from the pumping region directly to the lower part of their frequency spectrum. We confirm several predictions of the newly-developed nonlinear theory of BEc of quasiparticles.

II. BEC IN THERMODYNAMIC EQUILIBRIUM: ANALYTICAL BACKGROUND

The physics of a BEC in systems with a flux equilibrium is, in many aspects, similar to that of a BEC in thermodynamic equilibrium. Therefore, to stress the similarities and differences of basic physics in these two regimes, it is useful to use the same or similar notations. To introduce these notations, we shortly describe the BEC process in wave systems under consideration using a customary framework (see, e.g. [12, 24–27]).

A. Bose-Einstein and Rayleigh-Jeans distributions

It is well known from various textbooks (see, e.g. [28]) that the free evolution of an ideal Bose gas and weakly-interacting wave systems results in the BE distribution for particle (e.g. ^{4}He atom) or quasiparticle numbers:

$$n_k^{\mathrm{BE}} = \frac{1}{\exp[(E_k-\mu)/T]-1}\,, \tag{4a}$$

in which E_k is the particle (or quasiparticle) energy, T is the temperature, and μ is the chemical potential. For non-relativistic particles and quasiparticles with parabolic dispersion law Eq.(1b), to ensure $T > 0$ and $n_k \geq 0$ the value of μ must be smaller than the minimum of E_k: $\mu \leq E_0$.

In the low-energy limit, when $(E_k - \mu) < T$, the BE distribution approaches its classical limit, known as the Rayleigh-Jeans (RJ) distribution [28]:

$$n_k^{\mathrm{RJ}}(T,\mu) = \frac{T}{E_k-\mu}\,. \tag{4b}$$

In the opposite limit, when $E_k - \mu > T$, the BE distribution (4a) becomes exponentially small:

$$n_k^{\mathrm{BE}} \to \exp[-(E_k-\mu)/T]\,. \tag{4c}$$

We can understand the crossover wave number $k_\times$, defined by the equation

$$T = \frac{(\hbar k_\times)^2}{2m} + E_0 - \mu\,, \tag{4d}$$

as a quantum cutoff of the classical RJ-distribution (4b): for $k > k_\times$ it becomes exponentially small according to Eq. (4c).

Note that the crossover wave number $k_\times$ may exceed the maximal wave number $k_{\max} \simeq \pi/a_0$, determined by the inter-atomic scale a_0 or by some details of the system's dynamics (e.g. by the crossover between the flux- and the thermodynamic equilibrium regimes) as will be clarified below. For simplicity, in the present paper, we assume $k_{\max}$ to be greater than $k_\times$.

B. Quantum nature of a BEC of Bose-atoms and waves

To stress the quantum-mechanical nature of the BEC in both the ideal Bose gas and the gas of quasiparticles, we shortly recall here some results of the celebrated 1925 paper by Albert Einstein [2].

Consider the thermodynamic equilibrium in the systems characterized by the total number N_{tot} of ^{4}He atoms or quasiparticles and the total energy E_{tot}, measured for quasiparticles from their energy gap E_0:

$$N_{\mathrm{tot}} = \int \frac{n_{\boldsymbol{k}}^{\mathrm{BE}}\, d^d k}{(2\pi)^d} \Rightarrow \frac{1}{2\pi^2}\int_0^{k_\times} n_{\boldsymbol{k}}^{\mathrm{RJ}}\, k^2 dk\,, \tag{5a}$$

$$E_{\mathrm{tot}} = \int \frac{(\hbar k)^2}{2\,m}\frac{n_{\boldsymbol{k}}^{\mathrm{BE}}\, d^d k}{(2\pi)^d} \Rightarrow \frac{\hbar^2}{4\pi^2 m}\int_0^{k_\times} n_{\boldsymbol{k}}^{\mathrm{RJ}}\, k^4 dk\,. \tag{5b}$$

Here, $n_{\boldsymbol{k}}^{\mathrm{BE}}$ is the BE distribution, given by Eq. (4a), $dk^d = 4\pi k^2 dk$ in the isotropic 3D case considered here with the dimensionality $d = 3$, and m is either the actual mass of ^{4}He atoms or the effective mass of quasiparticles. To estimate the integrals in Eqs. (5), we replaced $n_{\boldsymbol{k}}^{\mathrm{BE}}$ in the rightmost integrals by $n_{\boldsymbol{k}}^{\mathrm{RJ}}$ and accounted for the exponential decay of $n_{\boldsymbol{k}}^{\mathrm{BE}}$ above the quantum cutoff (i.e. for $k > k_\times$) by introducing the upper limit of integration $k_\times$.

The two relations (5) allow us to find T and μ in the final equilibrium state. However, the direct substitution of n_k^{RJ} into Eqs. (5) leads to an immediate problem, known

as the ultraviolet catastrophe: both integrals for $N_{\rm tot}$ and $E_{\rm tot}$ diverge for $k_\times \to \infty$:

$$N_{\rm tot} \approx \frac{T}{2\pi^2}\int\limits_0^{k_\times} \frac{k^2 dk}{(\hbar k)^2/(2m) + E_0 - \mu}\,, \tag{6a}$$

$$E_{\rm tot} \approx \frac{\hbar^2\, T}{4\pi^2 m}\int\limits_0^{k_\times} \frac{k^4 dk}{(\hbar k)^2/(2m) + E_0 - \mu}\,. \tag{6b}$$

The only solution is to account for the finite value of the quantum cutoff $k_\times$, i.e. for the quantum character of the problem.

A simple analysis of Eqs. (6) shows that lowering $E_{\rm tot}$ with fixed $N_{\rm tot}$ leads to smaller T, while μ increases and approaches E_0, which is zero for ^{4}He atoms or $\hbar\omega_0$ for quasiparticles. As μ reaches E_0, Eq. (6a) gives an estimate of the maximal possible number of excited "gaseous" ^{4}He atoms or quasiparticles with $E_k > E_0$, which we denote as $N_{\rm gas}$:

$$N_{\rm gas} \approx \frac{k_\times^3}{4\pi^2}\,, \quad k_\times = \frac{\sqrt{2mT}}{\hbar}\,. \tag{7a}$$

The corresponding parameter $E_{\rm tot}$ we denote as $E_{\rm gas}$. According to Eq. (6b) we find:

$$E_{\rm gas} \approx N_{\rm gas}\frac{(\hbar k_\times)^2}{6m} \approx \frac{\pi^{4/3}\hbar^2}{3\cdot 2^{1/3} m}\big(N_{\rm gas}\big)^{5/3}\,. \tag{7b}$$

For $E_{\rm tot} < E_{\rm gas}$, the number of "gaseous" ^{4}He atoms or quasiparticles at the excited energy levels $N_{\rm gas}$ becomes smaller than their total number $N_{\rm tot}$. What happens with their excess number $N_{\rm tot} - N_{\rm gas}$? The answer was given by Einstein in Ref. [2]: the excess ^{4}He atoms (and quasiparticles, as we understand now) occupy only ONE level with the minimal energy, independently of the size of the system, forming a BEC, in which the number of BE condensed atoms or quasiparticles $N_{\rm BEC} = N_{\rm tot} - N_{\rm gas}$ is macroscopically large. All these BE condensed quasiparticles belong to the basic quantum state with its wave function coherent over the entire size of the system, owing to the fundamental principle of quantum mechanics of the indistinguishability of identical quasiparticles: the particles (or quasiparticles) with zero and natural spins can occupy any quantum state without limitation of their occupation number.

The existence of the quantum cutoff and the indistinguishability of identical (quasi)particles are necessary conditions for the BE condensation of Bose atoms and quasiparticles. Therefore, the phenomenon of the BE condensation of ^{4}He atoms and other Bose atoms, as well as magnons and other quasiparticles, has a fundamentally quantum nature.

C. Quasi-BEC in two-dimensional systems

In the 2D isotropic case, $d^2k = 2\pi k dk$ and integrals for $N_{\rm tot}$ and $E_{\rm tot}$, similar to Eqs. (6), take the form:

$$\begin{aligned} N_{\rm tot} \approx& \frac{T}{2\pi}\int\limits_0^{k_\times} \frac{k dk}{(\hbar k)^2/(2m) - \delta\mu} = \frac{k_\times^2}{4\pi}\ln\Big(1 - \frac{T}{\delta\mu}\Big) \\ \approx& \frac{k_\times^2}{4\pi}\ln\Big(\frac{T}{|\delta\mu|}\Big) = \frac{k_\times^2}{2\pi}\ln\Big(\frac{k_\times}{k_{\rm min}}\Big)\,, \end{aligned} \tag{8a}$$

$$\begin{aligned} E_{\rm tot} \approx& \frac{\hbar^2\, T}{8\pi^2 m}\int\limits_0^{k_\times} \frac{k^3 dk}{(\hbar k)^2/(2m) - \delta\mu} \\ =& \frac{k_\times^2}{4\pi}\Big[T + \delta\mu\ln\Big(1 + \frac{T}{\delta\mu}\Big)\Big] \approx \frac{T k_\times^2}{4\pi}\,, \text{ where} \end{aligned} \tag{8b}$$

$$\delta\mu \equiv \mu - E_0 < 0\,, \text{ and } k_{\rm min} \equiv \frac{\sqrt{2m|\delta\mu|}}{\hbar}\,. \tag{8c}$$

As $\delta\mu \to 0$, $N_{\rm tot}$ becomes logarithmically large, i.e., any large number of quasiparticles can occupy excited levels with $k > 0$. Therefore, BE condensation never happens in unbounded 2D media.

According to Eqs. (1) and (4b), for $\mu = E_0 = \hbar\omega_0$ the wave distribution diverges at $k = 0$:

$$n_k^{\rm RJ} = \frac{T}{\hbar\omega_0 (ak)^2} = \frac{2mT}{(\hbar k)^2} \tag{9a}$$

and formally $N_{\rm tot} = \infty$. Nevertheless, when $N_{\rm tot} \to \infty$ but still finite, $\mu \to \hbar\omega_0$, and $k_{\rm min} \to 0$, the coherence length of the quasiparticles

$$\ell \simeq \pi/k_{\rm min} \tag{9b}$$

increases and finally reaches the sample size. In other words, the wave system becomes coherent across the entire sample and can be practically considered as a BEC. Nevertheless, to be formally rigorous, we will refer to this system as quasi-BEC [25].

III. FLUX EQUILIBRIUM WITH WEAK PUMPING: QUASI-EQUILIBRIUM REGIME

In this Section we consider an isotropic system with a parabolic dispersion law Eq. (1) and relatively weak pumping, such that in the stationary case the system can be considered close to the thermodynamic equilibrium. Then, similar to the equilibrium regime, main contributions to all $N_{\rm tot}$- and $E_{\rm tot}$-integrals, given by Eqs. (5), come from the range $k < k_\times$, i.e., below the crossover between the quantum and classical scales. To simplify the appearance of our results, we approximate, analogous to the previous Sec. II B, the BE distribution (4a) in this range by the Rayleigh-Jeans distribution (4b).

The idea of the theoretical analysis of the BE condensation in the quasi-equilibrium regime is simple. By balancing the rate of the quasiparticle input with the rate

of their loss, we will find their total number $N_{\rm tot}$ in the flux-equilibrium regime. A similar analysis of the rate equation for the energy allows us to find the total energy of the system $E_{\rm tot}$. Because the system is assumed to be close to the thermodynamic equilibrium in the vicinity of the energy minimum, we can find an effective temperature $T_{\rm eff}$, describing a local Rayleigh-Jeans distribution in this region. In turn, this allows us to find the number of excited quasiparticles $N_{\rm gas}$, occupying energy levels $E_k > E_0$. If $N_{\rm gas}$ turns out to be smaller than $N_{\rm tot}$, the excess quasiparticles create the BEC: $N_{\rm tot} - N_{\rm gas} = N_{\rm BEC}$. Otherwise, there is no BEC.

A. BEC in 3D-systems

To study BE condensation in 3D systems along the lines of the suggested procedure, consider now the continuity equation for the quasiparticle numbers $n_{\boldsymbol{k}}$ with a damping frequency γ (taken for simplicity as $\boldsymbol{k}$-independent) and a source (influx) of quasiparticles f at a surface of the sphere of radius $k_{\rm f}$:

$$\frac{k^2}{2\pi^2}\frac{\partial n_k}{\partial t} + \frac{\partial \eta_k}{\partial k} = -\frac{\gamma k^2}{2\pi^2}\, n_k + \frac{k_{\rm f}^2 f}{2\pi^2}\delta(k-k_{\rm f})\ . \qquad (10)$$

Here η_k is the flux of quasiparticles in the 1D-space of $k = |\boldsymbol{k}|$ (the angle-averaged 3D $\boldsymbol{k}$-space),

The rate equation for the energy (measured from E_0)is obtained by multiplying Eq. (10) by $\hbar\delta\omega_k = \hbar\,\omega_0 a^2 k^2$. Integrating the result, we obtain for the total energy in 3D:

$$E_{\rm tot}^{\rm 3D} = \frac{\hbar\omega_0 a^2 f k_{\rm f}^4}{2\pi^2\gamma}\ . \qquad (11a)$$

Now, using the definition Eq. (1d) and in analogy to Eq. (6b) with the effective temperature $T = T_{\rm eff}$ and the effective mass $m = m_{\rm eff}$, as well as assuming the presence of the BEC (i.e. $\mu = E_0$), we rewrite $E_{\rm tot}$ as:

$$E_{\rm tot}^{\rm 3D} = \frac{T_{\rm eff} k_\times^3}{6\pi^2}\ . \qquad (11b)$$

Equations (11) allows us to find $T_{\rm eff}$. Using it to find, with the help of Eq. (6a), the total number of exited (gaseous) quasiparticles with $k > 0$ we obtain:

$$N_{\rm gas}^{\rm 3D} = \frac{T_{\rm eff}\, k_\times}{2\pi^2\hbar\, a^2\,\omega_0} = \frac{3 f k_{\rm f}^4}{2\pi^2 k_\times^2\gamma}\ . \qquad (12)$$

On the other hand, the total number of quasiparticles $N_{\rm tot}$ can be found by integration of the particle rate Eq. (10):

$$N_{\rm tot}^{\rm 3D} = \frac{f\, k_{\rm f}^2}{2\pi^2\gamma}\ . \qquad (13)$$

The excess of $N_{\rm tot}^{\rm 3D}$ over $N_{\rm gas}$ is the number of BE condensed quasiparticles:

$$N_{\rm BEC}^{\rm 3D} = N_{\rm tot}^{\rm 3D} - N_{\rm gas}^{\rm 3D} = \frac{f k_{\rm f}^2}{2\pi^2\,\gamma}\Big(1 - \frac{k_{\rm f}^2}{k_{\rm cr}^2}\Big)\,, \quad k_{\rm cr}^2 \equiv \frac{k_\times^2}{3}\ . \qquad (14)$$

Recall that by setting $\mu = E_0$ we assumed that the BEC is formed, i.e., $N_{\rm BEC}^{\rm 3D} > 0$. We see that the BEC appears only if the spectral location of the quasiparticle influx f is below the critical value $k_{\rm cr}$, which is independent of the value of f. However, if the condition $k_{\rm f} < k_{\rm cr}$ is fulfilled, the particle number in the BEC is proportional to f/γ. The numerical factor 3 in Eq. (14) is a consequence of the simplifying assumption that γ_k is k-independent.

The requirement of the smallness of $k_{\rm f}$ for BE condensation has a simple physical meaning. In our model with monochromatic pumping [at a single frequency $\omega(k_{\rm f})$] of the energy (counted from E_0) and the quasiparticles, their influxes, $P_{_E}$ and $P_{_N}$ are related: $P_{_E} = \hbar[\omega(k_{\rm f}) - \omega(0)]P_{_N}$. This means that at the constant quasiparticle influx $P_{_N}$ (and, consequently, constant $N_{\rm tot}^{\rm 3D}$), the energy influx $P_{_E}$, being proportional to $k_{\rm f}^2 P_{_N}$, decreases with decreasing $k_{\rm f}$. Accordingly, $E_{\rm tot}$ and $T_{\rm eff}$ also decrease with decreasing $k_{\rm f}$. Clearly, the wave system with the constant $N_{\rm tot}$ will unavoidably experience BE condensation when $k_{\rm f}$ (and consequently $T_{\rm eff}$) become smaller and smaller. On the other hand, for large $k_{\rm f}$ in the hot system there will be no BEC. Hence, there is a critical value $k_{\rm f} = k_{\rm cr}$, Eq. (14), at which BE condensation happens.

B. Quasi-BEC in 2D-systems

As we discussed in Sec. II C, one expects the appearance of a quasi-BEC in a finite-size 2D-space, say in a square domain $L \times L$. Assuming for concreteness periodical boundary conditions, we end up with a discrete $\boldsymbol{k}$-space, in which $k_x = \pm 2\pi n_x/L$ and $k_y = \pm 2\pi n_y/L$ with n_x and $n_y = 0\,, 1\,, 2\,, \ldots L$. The wave vector $\boldsymbol{k} = 0$, i.e. $k_x = k_y = 0$, can be considered as the position of the quasi-BEC, while the rest of the $\boldsymbol{k}$-space can be roughly approximated as a continuous $\boldsymbol{k}$-space, restricted by the inequality $k > \widetilde{k}_{\rm min} \approx 2\pi/L$. If so, the quasiparticle distribution in 2D case reads:

$$n_k = \frac{T\theta(k_{\rm min})}{\hbar\,\omega_0(a\,k)^2} + (2\pi)^2 N_{\rm BEC}\delta^2(\boldsymbol{k})\,, \quad k < k_\times\ , \qquad (15)$$

where $\theta(k_{\rm min})$ is the Heaviside step function.

The 2D version of the quasiparticle rate equation (10) is:

$$\frac{k}{2\pi}\frac{\partial n_k}{\partial t} + \frac{\partial \eta_k}{\partial k} = -\frac{\gamma k}{2\pi}\, n_k + \frac{k_{\rm f} f}{2\pi}\delta(k-k_{\rm f})\ . \qquad (16)$$

Multiplying the stationary version of this equation by $\hbar\,\omega_0 a^2 k^2$ and integrating over dk gives for the total energy

$$E_{\rm tot}^{\rm 2D} = \frac{\hbar\omega_0 f\, a^2 k_{\rm f}^3}{2\pi\gamma}\,, \qquad (17a)$$

similar to Eq. (11a). By analogy with Eq. (6b), $E_{\rm tot}^{\rm 2D}$ in terms of the effective temperature reads

$$E_{\rm tot}^{\rm 2D} = \frac{T_{\rm eff} k_\times^2}{4\pi} \ . \tag{17b}$$

Similar to the 3D case, these equations allow one to find $T_{\rm eff}$ and, by the help of a 2D version of Eq. (6a), the total number of gaseous quasiparticles in 2D:

$$\begin{aligned} N_{\rm gas}^{\rm 2D} &= \frac{T_{\rm eff}}{2\pi\hbar\,\omega_0 a^2} \ln\Big(\frac{k_\times}{\widetilde{k}_{\rm min}}\Big) \\ &= \frac{f k_{\rm f}^3}{k_\times^2 \gamma} \ln\Big(\frac{k_\times}{\widetilde{k}_{\rm min}}\Big) , \qquad \widetilde{k}_{\rm min} \approx \frac{2\pi}{L} , \end{aligned} \tag{18}$$

instead of Eq. (12) for the 3D case.

Now, integrating the stationary Eq. (16) over k, one gets a new equation for the total particle number $N_{\rm tot}^{\rm 2D}$ which gives, similar to Eq. (13) for $N_{\rm tot}^{\rm 3D}$:

$$N_{\rm tot}^{\rm 2D} = \frac{f k_{\rm f}}{2\pi\gamma} \ . \tag{19}$$

As in the 3D case, the excess of $N_{\rm tot}^{\rm 2D}$ over $N_{\rm gas}^{\rm 2D}$ gives the number of BE condensed quasiparticles:

$$N_{\rm BEC}^{\rm 2D} = N_{\rm tot}^{\rm 2D} - N_{\rm gas}^{\rm 2D} = \frac{f k_{\rm f}}{2\pi\,\gamma}\Big(1 - \frac{k_f^2}{k_{\rm cr}^2}\Big) , \tag{20a}$$

$$k_{\rm cr}^2 \equiv k_\times^2 \Big/ \Big[2 \ln\Big(\frac{k_\times}{\widetilde{k}_{\rm min}}\Big)\Big] \ . \tag{20b}$$

We see that also in 2D the BEC appears only if the position of the quasiparticle influx f is below the critical value $k_{\rm cr}$, now given by Eq. (20b). As before, $k_{\rm cr}$ is independent of the value of this influx f and $k_{\rm cr} < k_\times$. Also, similar to the 3D case, when $k_f < k_{\rm cr}$, the particle number in the BEC is proportional to f/γ.

IV. FLUX EQUILIBRIUM WITH STRONG PUMPING: SCALE-INVARIANT REGIMES

A. Kinetic equation and damping frequency

A consistent description of the evolution of an overpopulated wave system towards the formation of a BEC may be achieved in the framework of the theory of weak wave turbulence [27, 29]. The main tool of this theory is a kinetic equation (KE) for the occupation numbers $n(\boldsymbol{k})$ of quasiparticles:

$$\frac{\partial n_{\boldsymbol{k}}}{\partial t} = {\rm St}(\boldsymbol{k}, t) \ . \tag{21}$$

The collision integral ${\rm St}(\boldsymbol{k}, t)$ may be found by various ways [27, 29], including the Golden Rule, widely used in quantum mechanics [30]. In the case of the three-wave decay

$$\omega_{\boldsymbol{k}} = \omega_{\boldsymbol{1}} + \omega_{\boldsymbol{2}} , \quad \boldsymbol{k} = \boldsymbol{k}_1 + \boldsymbol{k}_2 , \tag{22a}$$

and confluence processes

$$\omega_{\boldsymbol{k}} + \omega_{\boldsymbol{1}} = \omega_{\boldsymbol{2}} , \quad \boldsymbol{k} + \boldsymbol{k}_1 = \boldsymbol{k}_2 , \tag{22b}$$

the collision integral takes the form [27, 29]:

$$\begin{aligned} {}^3{\rm St}(\boldsymbol{k}, t) = \pi \int d\boldsymbol{k}_1 d\boldsymbol{k}_2 \Big[\frac{1}{2} |V_{\boldsymbol{k}}^{\boldsymbol{12}}|^2 \, \mu_{\boldsymbol{k}}^{\boldsymbol{12}} \\ \times \delta(\boldsymbol{k} - \boldsymbol{k}_1 - \boldsymbol{k}_2) \delta(\omega_{\boldsymbol{k}} - \omega_{\boldsymbol{1}} - \omega_{\boldsymbol{2}}) \end{aligned} \tag{23a}$$

$$+ |V_{\boldsymbol{2}}^{\boldsymbol{k1}}|^2 \, \mu_{\boldsymbol{2}}^{\boldsymbol{k1}} \, \delta(\boldsymbol{k}_2 - \boldsymbol{k}_1 - \boldsymbol{k}) \delta(\omega_{\boldsymbol{k}_2} - \omega_{\boldsymbol{1}} - \omega_{\boldsymbol{k}}) \ . \tag{23b}$$

Here $\omega_j \equiv \omega_{k_j} \equiv \omega(k_j)$, $n_j \equiv n_{\mathbf{k}_j}$, $V_{\boldsymbol{k}}^{\boldsymbol{12}} \equiv V(\boldsymbol{k}, \boldsymbol{k}_1 \boldsymbol{k}_2)$ is the 3-wave interaction amplitude and $\mu_{\boldsymbol{k}}^{\boldsymbol{12}} \equiv n_{\boldsymbol{1}} n_{\boldsymbol{2}} - n_{\boldsymbol{k}}(n_{\boldsymbol{1}} + n_{\boldsymbol{2}})$.

If the three-wave processes (22) are suppressed or forbidden, the main role is played by four-wave $2 \Leftrightarrow 2$ processes

$$\omega_{\boldsymbol{k}} + \omega_{\boldsymbol{1}} = \omega_{\boldsymbol{2}} + \omega_{\boldsymbol{3}} , \quad \boldsymbol{k} + \boldsymbol{k}_1 = \boldsymbol{k}_2 + \boldsymbol{k}_3 \ . \tag{24a}$$

In this case, the collision integral reads [27, 29]:

$$\begin{aligned} {}^4{\rm St}(\boldsymbol{k}, t) = \frac{\pi}{4} \int d\boldsymbol{k}_1 d\boldsymbol{k}_2 d\boldsymbol{k}_3 \, \delta(\boldsymbol{k} + \boldsymbol{k}_1 - \boldsymbol{k}_2 - \boldsymbol{k}_3) \\ \times \delta(\omega_{\boldsymbol{k}} + \omega_{\boldsymbol{1}} - \omega_{\boldsymbol{2}} - \omega_{\boldsymbol{3}}) \, |W_{\boldsymbol{k1}}^{\boldsymbol{23}}|^2 \\ \times [n_{\boldsymbol{2}} n_{\boldsymbol{3}} (n_{\boldsymbol{k}} + n_{\boldsymbol{1}}) - n_{\boldsymbol{k}} n_{\boldsymbol{1}} (n_{\boldsymbol{2}} + n_{\boldsymbol{3}})] \ . \end{aligned} \tag{24b}$$

Here $W_{\boldsymbol{k1}}^{\boldsymbol{23}} = W_{\boldsymbol{k},\boldsymbol{k}_1}^{\boldsymbol{k}_2,\boldsymbol{k}_3} = W(\boldsymbol{k}, \boldsymbol{k}_1; \boldsymbol{k}_2, \boldsymbol{k}_3)$ is the four-wave interaction amplitude.

The kinetic equations (21), (23) and (24b) have a stationary thermodynamic equilibrium solution in the form of the RJ distribution (4b). To describe the evolution of the system close to the RJ distribution, Eq. (21) can be approximately reformulated as follows,

$$\frac{\partial n_{\boldsymbol{k}}}{\partial t} = \gamma_{\boldsymbol{k}} \big[n_{\boldsymbol{k}}^{\rm RJ} - n_{\boldsymbol{k}} \big] \tag{25}$$

where $\gamma_{\boldsymbol{k}}$ is proportional to the part of the collision integral that explicitly includes $n_{\boldsymbol{k}}$. In the case of four-wave processes (24a) with the collision integral (24b) we find:

$$\begin{aligned} {}^4\gamma_{\boldsymbol{k}} = \frac{\pi}{4} \int d\boldsymbol{k}_1 d\boldsymbol{k}_2 d\boldsymbol{k}_3 |W_{\boldsymbol{k1}}^{\boldsymbol{23}}|^2 \delta(\boldsymbol{k} + \boldsymbol{k}_1 - \boldsymbol{k}_2 - \boldsymbol{k}_3) \\ \times \delta(\omega_{\boldsymbol{k}} + \omega_1 - \omega_2 - \omega_3) [n_{\boldsymbol{1}}(n_{\boldsymbol{2}} + n_{\boldsymbol{3}}) - n_{\boldsymbol{2}} n_{\boldsymbol{3}}] \ . \end{aligned} \tag{26a}$$

According to Eq. (25), near the equilibrium

$$n_{\boldsymbol{k}} - n_{\boldsymbol{k}}^{\rm RJ} \propto \exp[-\,{}^4\gamma_{\boldsymbol{k}} t] \ .$$

Therefore, ${}^4\gamma_{\boldsymbol{k}}$ (26a) has a meaning of the damping (or relaxation) frequency in the four-wave scattering processes (24a). Close to and at equilibrium it is positive ${}^4\gamma_{\boldsymbol{k}} > 0$.

In general, the kinetic Eq. (21) with the collision term (24b) can be written as follows:

$$\frac{\partial n(\boldsymbol{k})}{\partial t} = \Phi(\boldsymbol{k}) - \gamma(\boldsymbol{k}) n(\boldsymbol{k}) , \tag{26b}$$

where $n(\boldsymbol{k}) \equiv n_{\boldsymbol{k}}$, $\gamma(\boldsymbol{k}) = {}^{4}\gamma(\boldsymbol{k})$ is given by Eq. (26a) and the source term has the form

$$\Phi(\boldsymbol{k}) = \frac{\pi}{4}\int d\boldsymbol{k}_1 d\boldsymbol{k}_2 d\boldsymbol{k}_3\, \delta(\boldsymbol{k}+\boldsymbol{k}_1-\boldsymbol{k}_2-\boldsymbol{k}_3) \times |W^{\boldsymbol{23}}_{\boldsymbol{k1}}|^2 \delta(\omega_{\boldsymbol{k}}+\omega_{\boldsymbol{1}}-\omega_{\boldsymbol{2}}-\omega_{\boldsymbol{3}})\, n_{\boldsymbol{1}} n_{\boldsymbol{2}} n_{\boldsymbol{3}}\ . \tag{26c}$$

In thermodynamic equilibrium $n_{\boldsymbol{j}} = n^{\mathrm{RJ}}_{\boldsymbol{j}}$, $\Phi(\boldsymbol{k}) = \gamma(\boldsymbol{k}) n^{\mathrm{RJ}}_{\boldsymbol{k}}$ and Eq. (26b) coincides with Eq. (25), as expected.

B. Scale-invariant solutions of the kinetic equation

Weak wave turbulence theory [27, 29] also allows us to find stationary flux solutions of the KE in the isotropic scale-invariant case, for which the wave frequency depends only on $k = |\boldsymbol{k}|$ and the interaction amplitude $W^{\boldsymbol{23}}_{\boldsymbol{k1}}$ is a homogeneous function,

$$\omega_{\boldsymbol{k}} = \omega_k \propto k^{\alpha}\,, \qquad W^{\sigma\boldsymbol{k}_3,\sigma\boldsymbol{k}_4}_{\sigma\boldsymbol{k}_1,\sigma\boldsymbol{k}_2} = \sigma^m W^{\boldsymbol{k}_3,\boldsymbol{k}_4}_{\boldsymbol{k}_1,\boldsymbol{k}_2}. \tag{27}$$

Here, α is the frequency scaling index (for example, for magnons at the beginning of the exchange-dominated dispersion branch $\alpha = 2$), m is the four-wave interaction-amplitude scaling index and σ is a positive constant. For simplicity, let us take

$$W^{\boldsymbol{34}}_{\boldsymbol{12}} = W_0 a^m (k_1 k_2 k_3 k_4)^{m/4}\ , \tag{28}$$

where W_0 is a constant. Up to now, our analysis has a general character, applicable to any nonlinear wave system. Below, having in mind the comparison of our predictions with spin waves in a ferromagnetic material, we choose the interaction parameters typical for this system for further discussion. In the ferromagnetic material, at sufficiently large k, the exchange interaction with $m = 2$ is dominant. In the low-k range, the dipole-dipole interaction dominates, with $m = 0$.

The scaling solutions (up to a dimensionless prefactor) read

$$n_\varepsilon(k) \simeq \frac{\varepsilon^{1/3}}{W_0^{2/3}(a\,k)^{x_\varepsilon}}\,, \quad x_\varepsilon = d + \frac{2m}{3}\,, \tag{29a}$$

$$n_\eta(k) \simeq \frac{\eta^{1/3}}{W_0^{2/3}(a\,k)^{x_\eta}}\,, \quad x_\eta = d + \frac{2m-\alpha}{3}\ . \tag{29b}$$

Here ε and η are the energy and the quasiparticle (magnon) number fluxes, and d is the dimensionality of the space.

C. Directions of the fluxes and realizability of the flux solutions in ferromagnets

Following the Fjørtoft argument [31], one can show (see, e.g. [27, 29]) that the energy flux solution (29a) is oriented toward large k ("direct energy cascade"), while the quasiparticle-flux solution (29b) flows toward small k ("inverse particle cascade"). This conclusion is based on the analysis of the energy and quasiparticle number balance in the stationary, scale-invariant, isotropic situation, in which the energy and the quasiparticles are pumped around some intermediate wave number k_{f} and dissipate at both very small $k_<$- and very large $k_>$-numbers: $k_< \ll k_{\mathrm{f}}$, $k_> \gg k_{\mathrm{f}}$.

Now we are going to verify that the scale-invariant solutions (29) do have the directions of the energy and magnon number fluxes that agree with the Fjørtoft argument.

For that, we analyze the behavior of these fluxes for the distributions $n(k) \propto k^{-x}$ with an arbitrary value of x. We expect that for a very steep spectrum, the fluxes will act to change it toward the equilibrium spectra. Therefore, for large and positive x, given that $n(k)$ decreases sharply toward larger wave numbers, we expect both ε and η fluxes to be positive, i.e., directed toward large k. On the other hand, for large negative x, when the spectra are growing toward high wave numbers, we expect $\varepsilon, \eta < 0$. Furthermore, both fluxes will be zero for both thermal equilibrium exponents $x^{\mathrm{TE}}_\eta = 2$ (because $n_{\mathrm{RJ}} \propto 1/\omega_k$) and $x^{\mathrm{TE}}_\varepsilon = 0$. In addition, the flux of magnons $\eta(x)$ vanishes for the pure energy flux spectrum with exponent x_ε given by Eq. (29a), and the energy flux $\varepsilon(x)$ vanishes for the pure particle flux exponent x_η, given by Eq. (29b). By continuity, the signs of both fluxes for all x are fully determined by their signs at infinity and the locations of their zero crossings. The fluxes vary in the manner schematically shown in Figs. 2(a) and (b) for the 2D and 3D case, respectively, with the exchange-dominated interaction with $m = 2$, and Figs. 2(c) and (d) for the 2D and 3D case, respectively, with the dipole-dipole dominated interaction with $m = 0$ [32].

First, we consider the exchange-dominated case in ferromagnets ($m = 2$) for which

$$x_\varepsilon = \frac{10}{3}\,, \quad x_\eta = \frac{8}{3}\,, \quad \text{for } d = 2\,, \tag{30a}$$

$$x_\varepsilon = \frac{13}{3}\,, \quad x_\eta = \frac{11}{3}\,, \quad \text{for } d = 3\ . \tag{30b}$$

We see in Figs. 2(a,b) that in both 2D and 3D at the spectral index $x = x_\varepsilon$, corresponding to the pure energy flux ($\frac{10}{3}$ and $\frac{13}{3}$ respectively), the energy flux is positive, $\varepsilon > 0$. Similarly, we see that for $x = x_\eta$, corresponding to the pure flux of magnons ($\frac{8}{3}$ and $\frac{11}{3}$ respectively), the flux of magnons is negative, $\eta < 0$. These findings are in full agreement with the Fjørtoft prediction.

In the dipole-dipole interaction-dominated case, when $m = 0$,

$$x_\varepsilon = 2\,, \quad x_\eta = \frac{4}{3}\,, \quad \text{for } d = 2\,, \tag{31a}$$

$$x_\varepsilon = 3\,, \quad x_\eta = \frac{7}{3}\,, \quad \text{for } d = 3\ . \tag{31b}$$

These exponents are the same as in the Nonlinear Schrödinger (NLS) equation, studied in Refs. [27, 33, 34]. Consequently, our schematic representation of the fluxes

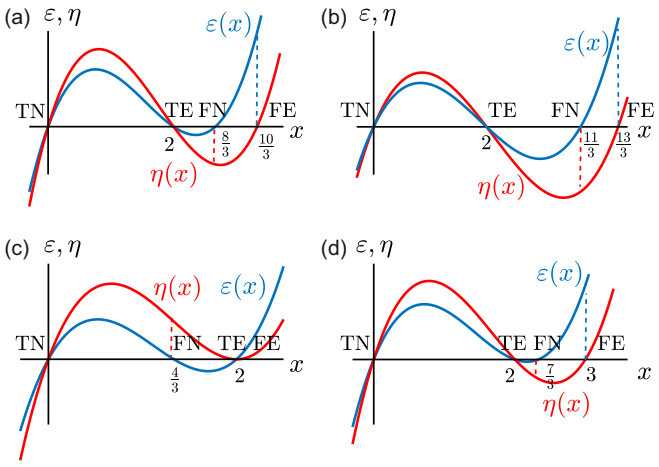

FIG. 2. Schematic presentation of the particle flux $\eta(x)$ (in red) and the energy flux $\varepsilon(x)$ (in blue) as a function of spectral index x. (a) exchange-dominated interaction, 2D; (b) exchange-dominated interaction, 3D; (c) dipole-dipole dominated interaction, 2D; (d) dipole-dipole dominated interaction, 3D.

Fig. 2(c,d) looks similar to Fig. 1(c,d) in Ref. [34]. For completeness, the analysis that led to the conclusions made in Ref. [34], is briefly reproduced below.

In 3D, ε is positive at x_η and η is negative at x_ε in agreement with the Fjørtoft argument. We therefore can expect that in 3D the Kolmogorov-Zakharov flux cascades with exponents (31b) are possible. A more detailed analysis [27, 33] shows that the inverse particle cascade Kolmogorov-Zakharov spectrum is indeed realized, while the direct energy cascade is marginally nonlocal and the respective spectrum must be modified by the logarithmic corrections.

As seen in Fig. 2(d), in spectra (29) the quasiparticles cascade is directed to large k and the energy cascade is zero. This contradicts the robust Fjørtoft-type analysis based on the energy and the quasiparticles number balance for the situation when the energy and quasiparticles are pumped around some intermediate wave number k_f and dissipate in both ranges of very small $k_<$- and very large $k_>$-numbers. The contradiction may be resolved if, instead of the pure scaling spectra (29), the inverse quasiparticles and the direct energy cascades are realized by spectra with a shape close the thermodynamic RJ equilibria (4b) with small corrections which take care of the magnon and energy fluxes toward small and large k, respectively.

D. Transition from 3D- to 2D-cases in thin films

In thin films, we chose the direction z orthogonal to the film surface. The corresponding wave vector is $k_z = \pi n_z/\Delta$, where Δ is the film thickness. Accordingly, the wave frequency is also quantized, and the frequency of the fundamental mode with $n_z = 1$ is separated from the frequency of the next mode with $n_z = 2$, etc. This results in the appearance of a crossover wave number $k_{2\leftrightarrow3}$ between the 2D and 3D regimes in the flux solutions. For $k \gg k_{2\leftrightarrow3}$, the 3D flux solutions can be realized, while for $k \ll k_{2\leftrightarrow3}$ the energy and quasiparticles exchange between waves with different n_z are strongly suppressed, or even forbidden. Roughly speaking, for $k_{2\leftrightarrow3}$ the frequency gap between waves with neighboring n_z is of the order of the interaction frequency (or damping frequency) of waves with $k \sim k_{2\leftrightarrow3}$.

For the problem at hand it means the following: if the pumping wave number strongly exceeds the crossover $k_\mathrm{f} \gg k_{2\leftrightarrow3}$, there exists a direct energy flux toward large k for $k > k_\mathrm{f}$, whereas in the intermediate range $k_{2\leftrightarrow3} < k < k_\mathrm{f}$, an inverse particle flux toward small k is realized. For small wave numbers $k < k_{2\leftrightarrow3}$, the wave system falls into the 2D regime, in which the scale-invariant flux solution cannot be realized. Instead, it approaches a solution close to the thermodynamic equilibrium with small deviations ensuring the required particle flux.

V. ULTRA-STRONG PUMPING: KINETIC INSTABILITY AND BEC

In this Section, we consider ultra-strong parametric pumping by an external monochromatic field of frequency ω_pump, exciting a very intense package of quasiparticles near the resonant frequency $\omega_\mathrm{par} = \omega_\mathrm{pump}/2$ according to Eq. (2), see Fig. 1. As predicted in Ref. [21], the scattering process with the conservation law

$$\omega(\boldsymbol{k}_\mathrm{par}) + \omega(\boldsymbol{k}'_\mathrm{par}) = \omega(\boldsymbol{k}_\mathrm{bot}) + \omega(\boldsymbol{k}_\mathrm{top})\,, \qquad (32)$$

shown in Fig. 3(a) decreases the damping frequency of the bottom and top waves $\gamma(\boldsymbol{k}_\mathrm{bot})$ and $\gamma(\boldsymbol{k}_\mathrm{top})$ such that they may become negative. If so, the cascade processes, discussed in Sec. IV B, may be augmented by a direct transfer of the parametrically injected quasiparticles to the lowest energy states, creating a dense cloud of incoherent "bottom" quasiparticles formed close to the BEC point [35] and a similar cloud at the high energy state ("top quasiparticles").

The linear stage of this phenomenon, referred to as kinetic instability [21–23, 36], is considered below in section V A. The exponential growth of the number of the

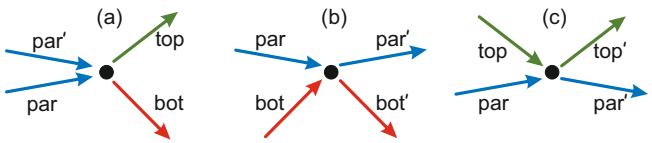

FIG. 3. (a) Interaction processes Eq. (32) leading to the kinetic instability. (b) and (c), scattering processes (33), leading to the widening of the frequency distribution of the bottom and top quasiparticles.

bottom and top quasiparticles due to kinetic instability alters the damping of the parametric ones. This process is discussed in V B. In its turn, two other scattering processes, shown in Figs. 3(b) and (c), involve parametric, bottom, and top waves

$$\begin{aligned}\omega(\boldsymbol{k}_{\rm par})+\omega(\boldsymbol{k}_{\rm bot})&=\omega(\boldsymbol{k}'_{\rm par})+\omega(\boldsymbol{k}'_{\rm bot})\,,\\ \omega(\boldsymbol{k}_{\rm par})+\omega(\boldsymbol{k}_{\rm top})&=\omega(\boldsymbol{k}'_{\rm par})+\omega(\boldsymbol{k}'_{\rm top})\,.\end{aligned}\tag{33}$$

It widens the frequency distribution of the bottom and top quasiparticles, as described in V C. Combining all processes together, we formulate the nonlinear description of the kinetic instability in V D.

Although the kinetic instability was first discovered in a system of parametrically excited magnons [21], it is a general physical phenomenon in nonlinear wave systems. To stress this generality and to clarify the underlying phenomena, we describe it here for the isotropic homogeneous wave system with the parabolic dispersion law (1a). We postpone the discussion of the specific features related to the anisotropic spectrum of magnons, shown in Fig. 7, until Sec. VI, which addresses the experimental study of magnon BEC formation in ferrimagnetic YIG.

A. Linear stage of the kinetic instability

To clarify the physics of the kinetic instability, we substitute the RJ distribution (4b) into Eq. (26a) for the damping frequency. We see that near the equilibrium $\gamma_{\boldsymbol{k}}>0$, meaning that the wave system, being close to the equilibrium, monotonically relaxes toward it. However, the right-hand-side (RHS) of Eq. (26a) has the negative term proportional to $n_{\boldsymbol{2}}n_{\boldsymbol{3}}$, which under some conditions may dominate.

To demonstrate this, let us conside the distribution as a sum of the equilibrium waves (4b) and a package of the parametric waves with $k=k_{\rm par}$ and total number $N_{\rm par}$. In the isotropic 3D case:

$$n(k)=n^{\rm RJ}(k)+n^{\rm par}(k)\,,\tag{34a}$$

$$n^{\rm par}(k)=\frac{N_{\rm par}}{4\pi k_{\rm par}^2}\delta(k-k_{\rm par})\,.\tag{34b}$$

Consequently, the rate Eqs. (26) for the bottom and top quasiparticles $n_{\rm bot}(k)$ and $n_{\rm top}(k)$ appearing in the scattering process (3), are as follows:

$$\begin{aligned}\frac{\partial n_{\rm bot}(k)}{\partial t}&=-\gamma_{\rm bot}(k)n_{\rm bot}(k)-\gamma_{\rm KI}(k)\big[n_{\rm bot}(k)+n_{\rm top}(k)\big]\,,\\ \frac{\partial n_{\rm top}(k)}{\partial t}&=-\gamma_{\rm top}(k)n_{\rm top}(k)-\gamma_{\rm KI}(k)\big[n_{\rm bot}(k)+n_{\rm top}(k)\big]\,.\end{aligned}\tag{35}$$

Here, $\gamma_{\rm bot}>0$ and $\gamma_{\rm top}>0$ are the original (positive) damping frequencies originating from the equilibrium quasiparticles $n^{\rm RJ}_{\boldsymbol{k}}$. The new terms, proportional to $\gamma_{\rm KI}(k)<0$, which leads to the kinetic instability, can be found from the last term $-n_{\rm par}(\boldsymbol{k}_2)n_{\rm par}(\boldsymbol{k}_3)$ in the RHS of Eq. (26a) for ${}^4\gamma_{\boldsymbol{k}}$ in both the bottom and the top quasiparticles

$$\begin{aligned}\gamma_{\rm KI}(k)=&-\frac{\pi}{4}\int d\boldsymbol{k}_1d\boldsymbol{k}_2d\boldsymbol{k}_3\delta(\boldsymbol{k}+\boldsymbol{k}_1-\boldsymbol{k}_2-\boldsymbol{k}_3)\\ &\times|W^{\boldsymbol{23}}_{\boldsymbol{k1}}|^2\delta(\omega_{\boldsymbol{k}}+\omega_1-\omega_2-\omega_3)n^{\rm par}(\boldsymbol{k}_2)n^{\rm par}(\boldsymbol{k}_3)\,.\end{aligned}\tag{36a}$$

As we see (following Ref. [21]), the value of $\gamma_{\rm KI}(k)$ is negative. For clarity of the presentation, it is convenient to introduce a positive object $\Gamma_{\rm KI}(k)=-\gamma_{\rm KI}(k)>0$ and to rewrite Eqs. (35) for the total number of the top and the bottom quasiparticles, $N_{\rm bot}=\int n_{\rm bot}(\boldsymbol{k})d\boldsymbol{k}$ and $N_{\rm top}=\int n_{\rm bot}(\boldsymbol{k})d\boldsymbol{k}$ as follows:

$$\begin{aligned}\frac{\partial N_{\rm bot}}{\partial t}&=\Gamma_{\rm KI}\big[N_{\rm bot}+N_{\rm top}\big]-\gamma_{\rm bot}N_{\rm bot}\,,\\ \frac{\partial N_{\rm top}}{\partial t}&=\Gamma_{\rm KI}\big[N_{\rm bot}+N_{\rm top}\big]-\gamma_{\rm top}N_{\rm top}\,.\end{aligned}\tag{36b}$$

Next, we integrate Eq. (36a) with respect to the directions of all $\boldsymbol{k}_j$. Using the procedure of averaging as in Refs. [33, 37], we conclude (up to a numerical prefactor) that

$$\begin{aligned}\Gamma_{\rm KI}\,(k)\simeq\frac{1}{k}\int dk_1dk_2dk_3k_1k_2k_3\,\min\{k,k_1,k_2,k_3\}|W^{\boldsymbol{23}}_{\boldsymbol{k1}}|^2\\ \times\delta(\omega_{\boldsymbol{k}}+\omega_1-\omega_2-\omega_3)n^{\rm par}(\boldsymbol{k}_2)n^{\rm par}(\boldsymbol{k}_3)\,.\end{aligned}\tag{36c}$$

Note that in our case $\min\{k,k_1,k_2,k_3\}=k$ which cancels against the prefactor of the integral $1/k$.

Substituting Eq. (34b) for $n^{\rm par}(\boldsymbol{k})$ we finally arrive at the following estimate for the positive contribution to the rate Eq. (36b), leading to the kinetic instability:

$$\Gamma_{\rm KI}(k)\simeq\frac{(\Omega^{\rm par}_W)^2}{\omega_{\rm par}}\,,\quad \Omega^{\rm par}_W\equiv|W_0|^2N_{\rm par}\,.\tag{37}$$

Here, we assume for simplicity that $W^{\boldsymbol{23}}_{\boldsymbol{k1}}=W_0$ in agreement with Eq. (28) with $m=0$ and we approximate $\omega_0(a\,k_{\rm par})^2\simeq\omega_{\rm par}$.

The linear Eqs. (36b) have exponential solutions

$$N_{\rm bot}(k,t)\propto\exp(\nu^{\pm}_k t)\,,\quad N_{\rm top}(k,t)\propto\exp(\nu^{\pm}_k t)\,,\tag{38a}$$

with

$$\begin{aligned}\nu^{\pm}_k=&\Gamma_{\rm par}-\frac{1}{2}\big(\gamma_{\rm top}+\gamma_{\rm bot}\big)\\ &\pm\frac{1}{2}\sqrt{\big(\gamma_{\rm top}-\gamma_{\rm bot}\big)^2+4\Gamma^2_{\rm KI}}\,.\end{aligned}\tag{38b}$$

The increment ν^+_k becomes positive if

$$\Gamma_{\rm KI}>\Gamma^{\rm th}_{\rm KI}=\frac{\gamma_{\rm top}\gamma_{\rm bot}}{\gamma_{\rm top}+\gamma_{\rm bot}}\simeq\gamma_{\rm bot},\ \text{for}\ \gamma_{\rm bot}\ll\gamma_{\rm top}.\tag{38c}$$

This condition may be fulfilled for low-frequency waves near the bottom of their frequency spectra, where $\gamma_{\rm bot}(k)$

is small. If so, these waves become unstable, and their numbers $N_{\rm bot}(t)$ and $N_{\rm top}(t)$ are related as follows,

$$N_{\rm bot}\Gamma_{\rm KI} = \frac{N_{\rm top}}{2}\Big[\gamma_{\rm top} - \gamma_{\rm bot} + \sqrt{\big(\gamma_{\rm top} - \gamma_{\rm bot}\big)^2 + 4\Gamma_{\rm KI}^2}\Big] \propto \exp(\nu_k^+ t)\ , \tag{39a}$$

and grow exponentially until the nonlinear effects become significant. The description of these effects is the subject of the Sec. V D.

Under stationary conditions, when $\nu_k^+ = 0$, the relationship between $N_{\rm bot}$ and $N_{\rm top}$ is even simpler:

$$N_{\rm bot}\gamma_{\rm bot} = N_{\rm top}\gamma_{\rm top}\ . \tag{39b}$$

Near the threshold $\Gamma_{\rm par} = \Gamma_{\rm par}^{\rm th}$, Eq. (38b) gives

$$\nu_k^+ \approx [\Gamma_{\rm KI}(k) - \Gamma_{\rm KI}^{\rm th}(k)]\frac{(\gamma_{\rm bot}+\gamma_{\rm top})^2}{\gamma_{\rm bot}^2+\gamma_{\rm top}^2} + \dots \tag{39c}$$

The condition $\nu_k^+ = 0$ defines the threshold of the kinetic instability if one neglects the scattering of the bottom and top quasiparticles on the parametric ones, considered in Sec. V C.

Using the estimate (37) for $\Gamma_{\rm par}$, we find from Eq. (38c) the critical value $N_{\rm par}^{\rm cr}$ corresponding to the threshold of the kinetic instability in which $\nu_k = 0$:

$$\pi|W|N_{\rm par}^{\rm cr} \simeq \sqrt{\omega_{\rm par}\,\gamma_{\rm bot}\gamma_{\rm top}/(\gamma_{\rm bot}+\gamma_{\rm top})}\ . \tag{40}$$

Corrections to this estimate caused by the scattering of the bottom and parametric quasiparticles will be discussed in Sec. V C.

B. Mean-field approximation for parametrically excited waves and feedback limitation of the kinetic instability

The statistical behavior of parametrically-excited waves in ferromagnets was intensively studied experimentally, theoretically and numerically since their discovery by Suhl in 1959 [38] and by Schlömann in 1962 [39]. A relatively simple theory of this phenomenon in the mean-field approximation, called the "S-theory", was developed later by Zakharov, L'vov and Starobinets, and presented in their review [40]. Further important achievements in this problem were summarised, for example, in the books [32, 41].

The evolution equations for the total number of parametrically-excited waves $N_{\rm par}$ and their mean phase $\Psi_{\rm par}$ (cf. Eqs. (5.4.13) of the book [32]) is our starting point. Here we augment them with the new term $\Gamma_{\rm par}N_{\rm par}$, which describes the loss of parametric waves due to their direct transfer to the bottom and the top waves by the kinetic instability described below.

In the spherically symmetric case, these equations take the form

$$\frac{dN_{\rm par}}{dt} = \big(hV\sin\Psi_{\rm par} - \gamma_{\rm par} - \Gamma_{\rm par}\big)N_{\rm par}\ , \tag{41a}$$

$$\frac{d\Psi_{\rm par}}{dt} = hV\cos\Psi_{\rm par} + \Omega_S\ , \quad \Omega_S \equiv SN_{\rm par}\ , \tag{41b}$$

Here, h is the amplitude of the external homogeneous oscillating field, V is the interaction amplitude of this field with the parametric waves, $\gamma_{\rm par}$ is their damping frequency, and S is the mean interaction amplitude of a pair of parametric waves with opposite wave vectors $\pm\boldsymbol{k}_{\rm par}$, with another pair $\pm\boldsymbol{k}'_{\rm par}$:

$$S = \Big\langle W^{\boldsymbol{k}'_{\rm par},-\boldsymbol{k}'_{\rm par}}_{\boldsymbol{k}_{\rm par},-\boldsymbol{k}_{\rm par}}\Big\rangle\ . \tag{41c}$$

To estimate the additional damping $\Gamma_{\rm par}$, consider KE (21) with the collision term ${}^4{\rm St}(\boldsymbol{k},t)$, given by Eq. (24b), with the resonance conditions (24a), in which we take $\boldsymbol{k} = \boldsymbol{k}_{\rm par}$, $\boldsymbol{k}_1 = \boldsymbol{k}'_{\rm par}$, (where $|\boldsymbol{k}_{\rm par}| = |\boldsymbol{k}'_{\rm par}| = k_{\rm par}$), $\boldsymbol{k}_2 = \boldsymbol{k}_{\rm bot}$, $\boldsymbol{k}_3 = \boldsymbol{k}_{\rm top}$ or $\boldsymbol{k}_3 = \boldsymbol{k}_{\rm bot}$, $\boldsymbol{k}_2 = \boldsymbol{k}_{\rm top}$.

The last choice gives the same contribution as the previous one and can be accounted for by replacing the numerical prefactor $\pi/4 \to \pi/2$. Corresponding values of the frequencies are as follows: $\omega_k = \omega_1 = \omega_{\rm par}$, $\omega_2 = \omega_{\rm bot}$, $\omega_3 = \omega_{\rm top}$. This way we get

$$\Gamma_{\rm par}(k_{\rm par}) \simeq \frac{\pi}{2}\int d\boldsymbol{k}_1 d\boldsymbol{k}_2 d\boldsymbol{k}_3\,\delta(\boldsymbol{k}_{\rm par}+\boldsymbol{k}_1-\boldsymbol{k}_2-\boldsymbol{k}_3) \times \delta(2\omega_{\rm par}-\omega_{\rm bot}-\omega_{\rm top})\,|W^{\boldsymbol{23}}_{\boldsymbol{k1}}|^2 \times n_{\rm par}(\boldsymbol{k}_1)\big[n_{\rm bot}(\boldsymbol{k}_2)+n_{\rm top}(\boldsymbol{k}_3)\big]\ . \tag{42a}$$

Note that the numerical prefactor here is twice as large as in Eq. (36a) for $\gamma_{\rm KI}(k)$. Estimating $\Gamma_{\rm par}(k_{\rm par})$ from Eq. (42a), in the same way we obtained the estimate (37) for $\Gamma_{\rm KI}(k)$ from Eq. (36a), we finally get:

$$\Gamma_{\rm par}(k_{\rm par}) \simeq \frac{2|W|^2N_{\rm par}N_+}{\omega_0(ak_{\rm par})^2} \simeq \frac{2|W|^2N_{\rm par}N_+}{\omega_{\rm par}}\ , \quad N_+ \equiv N_{\rm bot}+N_{\rm top}\ . \tag{43a}$$

Comparing this estimate with Eq. (37) for $\Gamma_{\rm KI}(k)$, we see that $N_{\rm par}\Gamma_{\rm par}$, the rate of dissipation of parametric waves due to the kinetic instability, is about $2N_{\rm bot}\Gamma_{\rm KI}N_+$, the total input rate of the bottom and top quasiparticles. A more detailed analysis shows that this relationship is exact. Namely, the positive contribution $\Gamma_{\rm par}$ to the rate Eq. (36b), leading to the kinetic instability, and the additional damping frequency $\Gamma_{\rm bot}^{\rm top}$ in Eq. (41a) are related as follows:

$$\Gamma_{\rm par}N_{\rm par} = 2\Gamma_{\rm KI}N_+\ . \tag{43b}$$

Both effects are caused by the same 4-wave scattering

$$\omega(\boldsymbol{k}_1)+\omega(\boldsymbol{k}_2) \Longrightarrow \omega(\boldsymbol{k}_3)+\omega(\boldsymbol{k}_4)\,, \tag{43c}$$

in which the "initial" waves with wave vector $\boldsymbol{k}_1$ and $\boldsymbol{k}_2$ are parametric waves with $\omega(\boldsymbol{k}_1) \simeq \omega(\boldsymbol{k}_2) \simeq \omega_{\rm pump}/2$,

while the "resulting" waves are the bottom and top quasiparticles with the frequencies $\omega_{\rm bot}$ and $\omega_{\rm top} = 2\omega_{\rm par} - \omega_{\rm bot}$.

From the quantum-mechanical viewpoint, one act of the scattering Eq. (43c) leads to the disappearing of two parametric quasiparticles and the creation of one bottom quasiparticle and one "top" quasiparticle with $\omega_{\rm top}$. Therefore, the corresponding damping $-\Gamma_{\rm par}N_{\rm par}$ in the rate Eq. (41a) for the parametric quasiparticles must be negative. Its modulus must be positive and exactly equal to the input contributions $2\,\Gamma_{\rm KI}N_+$ to the RHS of the sum of the rate Eqs. (35) for the bottom and top quasiparticles.

Equations (41) have the stationary solution

$$(SN_{\rm par})^2 = (hV)^2 - (\gamma_{\rm par} + \Gamma_{\rm par})^2 \ . \tag{44}$$

Furthermore, Eqs. (43a), (43b) and (44) allow us to find $N_{\rm par}$ for a given hV and N_+ for a given hV and $N_{\rm par}$:

$$N_{\rm par} = \frac{\omega_{\rm par}}{\omega_{\rm par}^2 S^2 + 4W^4 N_+^2}\Big[-\gamma_{\rm par}W^2N_+ + \sqrt{(hV)^2\big(\omega_{\rm par}^2S^2 + W^4N_+^2\big) - \gamma_{\rm par}^2\omega_{\rm par}^2S^2}\Big] , \tag{45a}$$

$$N_+ = \frac{\omega_{\rm par}}{W^4N_{\rm par}^2}\Big[-\gamma_{\rm par}W^2N_{\rm par} + \sqrt{(hVW^2N_{\rm par})^2 - S^2(WN_{\rm par})^4}\Big] \ . \tag{45b}$$

Using Eq. (39b), one easily reconstructs $N_{\rm bot}$ and $N_{\rm top}$ from N_+:

$$N_{\rm bot} = \frac{N_+\gamma_{\rm top}}{\gamma_{\rm bot}+\gamma_{\rm top}} \ , \quad N_{\rm top} = \frac{N_+\gamma_{\rm bot}}{\gamma_{\rm bot}+\gamma_{\rm top}} \ . \tag{45c}$$

Below the threshold of the kinetic instability, when $N_+ = 0$, Eq. (45a) simplifies to

$$|S|N_{\rm par} = \sqrt{(hV)^2 - \gamma_{\rm par}^2} \ . \tag{45d}$$

In addition, the threshold amplitude $h_{\rm th}$ of the parametric instability (for which $N_{\rm par} = N_+ = 0$) reads

$$h_{\rm th}V = \gamma_{\rm par} \ . \tag{45e}$$

C. Scattering of the bottom and parametric waves

In the nonlinear theory of kinetic instability, we have to account for one more process: scattering of the bottom or top quasiparticles on the intense parametric quasiparticles with the conservation law (24a), in which $\omega_1 \simeq \omega_2 \simeq \omega_{\rm par}$ and $\omega_{\boldsymbol{k}} \simeq \omega_{\boldsymbol{3}} \simeq \omega_{\rm bot}$ or $\omega_{\boldsymbol{k}} \simeq \omega_{\boldsymbol{3}} \simeq \omega_{\rm top}$:

$$\omega(k_{\rm bot}) + \omega(k_{\rm par}) = \omega(k'_{\rm bot}) + \omega(k'_{\rm par}) \ . \tag{46}$$

To do this, we have to account for an additional term $\mathrm{St}_{\rm scat}$ in the RHS of the rate Eq. (35):

$$\frac{\partial n_{\boldsymbol{k}}}{\partial t} = \nu_{\boldsymbol{k}}^+ n_{\boldsymbol{k}} + \mathrm{St}_{\rm scat}(\boldsymbol{k}) \, , \tag{47a}$$

where $\nu_{\boldsymbol{k}}^+$ is given, with required accuracy, by Eq. (39c) and

$$\mathrm{St}_{\rm scat}(\boldsymbol{k}) = \frac{\pi}{4}\int d\boldsymbol{k}_1 d\boldsymbol{k}_2 d\boldsymbol{k}_3 |W^{\boldsymbol{k}_2,\boldsymbol{k}_3}_{\boldsymbol{k},\boldsymbol{k}_1}|^2 n_{\rm par}(\boldsymbol{k}_1) \times n_{\rm par}(\boldsymbol{k}_2)\delta(\omega_{\boldsymbol{k}} + \omega_{\boldsymbol{1}} - \omega_{\boldsymbol{2}} - \omega_{\boldsymbol{3}}) \times (n_{\boldsymbol{3}} - n_{\boldsymbol{k}})\delta(\boldsymbol{k} + \boldsymbol{k}_1 - \boldsymbol{k}_2 - \boldsymbol{k}_3) \ . \tag{47b}$$

In Eq. (47a) and below in this section, $n_{\boldsymbol{k}}$ should be understood as $n_{\rm bot}(\boldsymbol{k})$ or $n_{\rm top}(\boldsymbol{k})$. This term originates from the collision term ${}^4\mathrm{St}(\boldsymbol{k},t)$ [Eq. (24b)], in which we account only for the leading terms $n_{\rm par}(\boldsymbol{k}_1)n_{\rm par}(\boldsymbol{k}_2)$ with the frequencies $\omega_1 \simeq \omega_2 \simeq \omega_{\rm par}$.

In the isotropic case, following Refs. [33, 37], we can rewrite Eqs. (47) in the ω-representation:

$$\frac{\partial n_\omega}{\partial t} = \nu_\omega^+ n_\omega + \int d\omega_1 d\omega_2 d\omega_3 \, \mathcal{S}(\omega,\omega_1,\omega_2,\omega_3) \times\delta(\omega+\omega_1-\omega_2-\omega_3)\, n^{\rm par}_{\omega_1} n^{\rm par}_{\omega_2}(n_{\omega_3} - \sqrt{\frac{\omega_3}{\omega}}\, n_\omega). \tag{48a}$$

Here ω and k are related by Eq. (1a): $\omega = \omega_0[1 + (ak)^2]$, and the particle number densities in the k- and ω-spaces, n_k and n_ω, in isotropic case are related as follows,

$$n_\omega = \frac{2\pi k}{\omega_0 a^2}\, n_k \ . \tag{48b}$$

It is important to take into account that parametrically excited waves usually experience auto-oscillation with a characteristic frequency about $\Omega_{\rm s}$, given by Eq. (41b) [32]. Therefore, in the ω-representation the distribution $n_{\rm p}(\omega)$ is not proportional to $\delta(\omega - \omega_{\rm p})$, but has some width Δ of the order of $\Omega_{\rm s}$ around $\omega_{\rm par}$. For concreteness, we assume the simple Gaussian form of $n^{\rm par}(\omega)$:

$$n^{\rm par}_\omega = \frac{N_{\rm par}}{\sqrt{2\pi}\Delta}\exp\Big[-\frac{(\omega-\omega_{\rm par})^2}{2\Delta^2}\Big] , \quad N_{\rm par} = \int\limits_{-\infty}^{\infty} n^{\rm par}_\omega d\omega \, , \quad \Delta \simeq \Omega_{\rm s} \simeq SN_{\rm par} \ . \tag{48c}$$

The collision integral in the RHS of Eq. (48a) is taken over the positive values ω_1, ω_2, and ω_3. The kernel of the integral (up to a dimensionless order-one constant) reads:

$$\mathcal{S}(\omega,\omega_1,\omega_2,\omega_3) \simeq \frac{\min\{\sqrt{\omega},\sqrt{\omega_1},\sqrt{\omega_2},\sqrt{\omega_3}\}}{\sqrt{\omega_1\omega_2\omega_3}}|W^{23}_{k,1}|^2 . \tag{49}$$

Substituting $n^{\rm par}_{\omega_1}$ and $n^{\rm par}_{\omega_2}$ from Eq. (48c) and keeping in mind that in this case $\omega \simeq \omega_3 \simeq \omega_0 < \omega_1 \simeq \omega_2 \simeq \omega_{\rm par}$ we conclude that

$$\mathcal{S}(\omega,\omega_1,\omega_2,\omega_3) \simeq \frac{|\mathcal{W}|^2}{\omega_{\rm par}} \, , \quad \mathcal{W} = W^{k_{\rm par}k_0,}_{k_0,k_{\rm par}} \ . \tag{50}$$

Furthermore, replacing the dummy variable ω_3 by $\widetilde{\omega}$ and integrating the resulting equation over ω_1 and ω_2,

we get (up to a numerical prefactor in the integral)

$$\frac{\partial n_\omega}{\partial t} = \nu_\omega^+ n_\omega + \frac{\Omega_W^2}{\omega_{\rm par}} \int_{\omega_0}^{\infty} \frac{d\widetilde{\omega}}{\Delta} (n_{\widetilde{\omega}} - n_\omega) \exp\Big[- \frac{(\omega - \widetilde{\omega})^2}{4\Delta^2} \Big] ,$$

$$\Omega_{\rm w} = \mathcal{W} N_{\rm par} \ . \tag{51}$$

Equation (51) was derived for the 3D case. In 2D, it has exactly the same form (51) but with a slightly different value of the numerical prefactor, which we are not controlling anyway.

Already at this stage, we can formulate an important consequence of Eq. (51): integrating it over ω from ω_0 to ∞ one gets a rate equation for the total number of bottom quasiparticles $N_{\rm bot}$ (or $N_{\rm top}$):

$$\frac{dN_{\rm bot}}{dt} = \left\langle \nu_\omega^+ \right\rangle N_{\rm bot} \, , \quad \left\langle \nu_\omega^+ \right\rangle \equiv \frac{\int_{\omega_0}^{\infty} \nu_\omega^+ n_\omega d\omega}{\int_{\omega_0}^{\infty} n_\omega d\omega} \ . \tag{52}$$

The integral term in Eq. (51) does not contribute to Eq. (52) due to the anti-symmetry of its integrand.

D. Nonlinear theory of the kinetic instability

Some aspects of the nonlinear theory of the kinetic instability were discussed a long time ago in Ref. [36] focusing only on the case of small super-criticality over the threshold of kinetic instability when $\Gamma_{\rm KI} - \Gamma_{\rm KI}^{\rm th} \ll \Gamma_{\rm KI}^{\rm th}$. Here, we extend this theory to the range of moderate and large super-criticality, i.e., when $\Gamma_{\rm KI} - \Gamma_{\rm KI}^{\rm th} \gtrsim \Gamma_{\rm KI}^{\rm th}$ or when $\Gamma_{\rm KI} \gg \Gamma_{\rm KI}^{\rm th}$.

The goal of the nonlinear theory of kinetic instability, developed here, is to find the spectral profile of the bottom quasiparticles n_ω, the total number of the parametric, bottom, and top quasiparticles, $N_{\rm par}$, $N_{\rm bot}$, and $N_{\rm top}$, as a function of the pumping amplitude h, accounting for the main interactions in the system only. The interactions among the parametric waves in the S-theory approximation are described in Sec. V B, the particle number flux from the parametric to the bottom quasiparticles – in Sec. V A and scattering of the bottom and parametric quasiparticles – in Sec. V C. At this stage, we neglect other nonlinear effects that might be important depending on the particular characteristics of the system at hand (e.g., the value and orientation of the external magnetic field, etc). The list of possibly important effects includes cascade mechanisms of particle transfer from the parametric and top quasiparticles to bottom ones, as described in Sec. IV, and nonlinear interactions in the system of the bottom quasiparticles, which can lead to the redistribution of the bottom quasiparticles and the growth of the damping frequency of the bottom quasiparticles with their number (see, e.g., Ref. [42] and book [32]).

1. *Narrow package approximation*

Assuming initially that the package n_ω is extremely narrow, such that ν_ω can be considered a constant, denoted $\nu_0 = \nu_{k_0}^+$, one obtains from Eq. (51):

$$\frac{dN_{\rm bot}}{dt} = \nu_0 N_{\rm bot} \, . \tag{53}$$

Below the kinetic instability threshold, when $\nu_0 < 0$, the total number of the bottom quasiparticles decays exponentially, and in the stationary condition $N_{\rm bot} = 0$ holds. Thus, according to Eq. (45d), $N_{\rm par}$ increases with the pumping amplitude hV, see Fig. 4, dashed light-blue line, until it reaches the value $N_{\rm par}^{\rm cr}$ given by Eq. (40).

The balance between the number of bottom and parametric quasiparticles is maintained by the increments ν^+ and $\Gamma_{\rm par}$. As $N_{\rm par} > N_{\rm par}^{\rm cr}$, the increment ν_k^+ becomes positive in a narrow range around k_0, and $N_{\rm bot}$ starts growing exponentially according to Eq. (39a). The bottom quasiparticles take energy from the parametric ones as described by the additional damping frequency $\Gamma_{\rm par}$ in the rate Eq. (41a) for the number of parametric quasiparticles $N_{\rm par}$. As a result, $N_{\rm par}$ drops back to $N_{\rm par}^{\rm cr}$ and the increment $\nu_{k_0}^+ \to 0$. Therefore, $N_{\rm par}$ becomes frozen at the level $N_{\rm par}^{\rm cr}$ for any $h > h^{\rm cr}$, see the horizontal dashed line in Fig. 4.

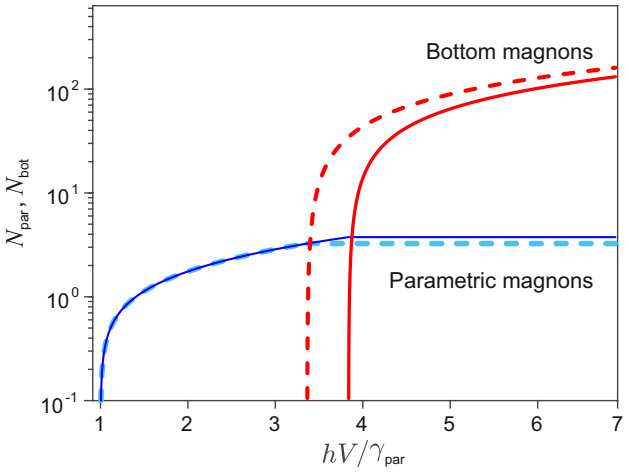

FIG. 4. Qualitative representation of the normalized number of parametric $SN_{\rm par}/\gamma_{\rm par}$ (light blue dashed line) and bottom quasiparticles $SN_{\rm bot}/\gamma_{\rm bot}$ (red dashed line) according to Eqs. (45). For concreteness, we took $S = W$, $\gamma_{\rm par} = \gamma_{\rm bot} \ll \gamma_{\rm top}$, $\omega_{\rm par} = 1000\gamma_{\rm par}$. Below the threshold of kinetic instability, $SN_{\rm par}/\gamma_{\rm par}$ is defined by Eq. (45d). Above the threshold, $SN_{\rm par}/\gamma_{\rm par}$ is frozen at its value at the threshold defined by Eq. (40). $N_{\rm bot}$ is a fraction of N_+ according to Eq. (45c). In its turn, N_+ as a function of h is defined by Eq. (45b) with $N_{\rm par} = N_{\rm par}^{\rm cr}$. Note that $N_{\rm bot} = 0$ for $h \le h_{\rm cr}$. Solid lines: the same, but accounting for the scattering of the bottom quasiparticles on the parametric ones in the framework of the exponential model (cf. Sec. V D 3). Here the spectral width of package is $\mathcal{D}_{\rm par} = 15$, giving $\lambda_0^{\rm mod} = 0.26$.

Substituting in Eq. (45b) $N_{\rm par} = N_{\rm par}^{\rm cr}$ from Eq. (40) and using Eq. (45d) for $h = h_{\rm cr}$, we obtain an equation for N_+ in which we assume for simplicity that $W = S > 0$

$$SN_+ = \frac{\omega_{\rm par}}{SN_{\rm par}^{\rm cr}}\Big[-\gamma_{\rm par}+\sqrt{\gamma_{\rm par}^2+V^2(h^2-h_{\rm cr}^2)}\Big]\,. \quad (54a)$$

For small super-criticality over the threshold of the kinetic instability $\delta h \equiv h - h_{\rm cr} \ll h_{\rm cr}$, one gets from Eq. (54a)

$$SN_+ \simeq SN_{\rm cr}\,\frac{\omega_{\rm par}}{\gamma_{\rm par}}\,\frac{\delta h}{h_{\rm cr}}\,. \quad (54b)$$

One sees from Fig. 4 that $N_{\rm bot}$ grows sharply just above $h^{\rm cr}$ as predicted by Eq. (54b): $N_{\rm bot}$ reaches the level of $N_{\rm par}^{\rm cr}$ (crossing of the blue and red lines) for very small $(\delta h/h_{\rm cr}) \simeq \gamma_{\rm par}/\omega_{\rm par} \ll 1$.

Now, we include the scattering of the bottom quasiparticles on the parametric ones, as described by the integral term in Eq. (51). Then Eq. (52) is identical to Eq. (53) upon replacement of ν_0 by the mean value $\langle\nu_\omega\rangle$. Due to the linearity of scattering Eq. (51), the profile of the bottom quasiparticles n_ω is independent of their total number $N_{\rm bot}$. Instead, it depends only on the number of the parametric quasiparticles $N_{\rm par}$, which is constant for $h > h^{\rm cr}$. Therefore, in the estimation of $\Omega_{_W} = \mathcal{W}N_{\rm par}$ and $\Delta \simeq |S|N_{\rm par}$ in Eqs. (51) and (48c) we have to take $N_{\rm par} = N_{\rm par}^{\rm cr}$. Thus, we conclude that n_ω and $\langle\nu_\omega\rangle$ are h-independent for $h > h^{\rm cr}$.

2. *Numerical analysis of the particle rate equation*

To extend the nonlinear theory of the kinetic instability beyond the narrow package approximation, we studied the rate Eq. (51) numerically. It is convenient to do this by transforming Eq. (51) to the dimensionless form by introducing $\tau = \gamma_{\rm bot}t$, $\mathcal{D}_{\rm par} = \Delta/\gamma_{\rm bot}$, $x = (\omega-\omega_0)/\gamma_{\rm bot}$ and $y = (\widetilde{\omega}-\omega_0)/\gamma_{\rm bot}$:

$$\begin{aligned}\frac{\partial n_x}{\partial\tau} =&\lambda_x n_x + {\rm Int}_x\,,\\ {\rm Int}_x \equiv&\sqrt{\frac{2}{\pi}}\,\frac{\mathcal{A}}{\mathcal{D}_{\rm par}}\int\limits_0^\infty dy(n_y-n_x)\exp\Big[-\frac{(x-y)^2}{2\mathcal{D}_{\rm par}^2}\Big]\,.\end{aligned} \quad (55a)$$

Here, the dimensionless increment is $\lambda_x = \nu_\omega/\gamma_{\rm bot}(\omega_0)$. Assuming for concreteness $\gamma_{\rm bot}(\omega) \propto \omega$, i.e. $\gamma_{\rm bot}(\omega) = \gamma_{\rm bot}(\omega_0)\omega/\omega_0$, we have

$$\begin{aligned}\lambda_x =&\lambda_0 - \frac{x}{x_0}\,,\quad \lambda_0 \equiv \Big(\frac{N_{\rm par}}{N_{\rm par}^{\rm cr}}\Big)^2 - 1\,,\\ x_0 =&\frac{\omega_0}{\gamma_{\rm bot}(\omega_0)}\,.\end{aligned} \quad (55b)$$

Taking into account Eqs. (51), we estimate

$$\mathcal{A} \simeq \frac{\omega_{\rm par}}{4\pi\omega_0}\Big(\frac{W}{\widetilde{W}}\Big)^2 \quad (55c)$$

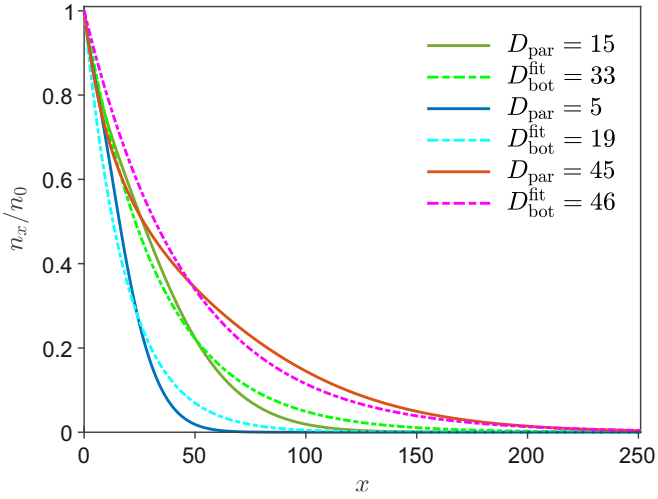

FIG. 5. Normalized stationary solutions of Eqs. (55a) n_x/n_0 for $\mathcal{D}_{\rm par} = 5$, (red line) $\mathcal{D}_{\rm par} = 15$, (blue line) and $\mathcal{D}_{\rm par} = 45$ (pink line) with $x_0 = 100$ and $\mathcal{A} = 1$. Respectively colored dashed lines show their approximated exponential fit with Eq. (56).

which is of the order of unity.

To get more detailed information about n_x and λ_0, we numerically solve Eq. (55a) together with the S-theory Eqs. (41) for n_ω using $\mathcal{D}_{\rm par} = 5, 15$ and 45, and taking for concreteness $x_0 = 100$. Resulting profiles of n_x are shown in Fig. 5 by color solid lines together with their approximate exponential fits,

$$n_x = \frac{1}{\mathcal{D}_{\rm bot}}\exp\Big(-\frac{x}{\mathcal{D}_{\rm bot}}\Big), \quad (56)$$

shown by dashed lines with matching colors. The values of $\lambda_0 = \lambda_0^{\rm num}$, corresponding to the stationary conditions, and $\mathcal{D}_{\rm bot} = \mathcal{D}_{\rm bot}^{\rm fit}$ for these three values of $\mathcal{D}_{\rm par}$ are given in the Tab. I.

1	$\mathcal{D}_{\rm par}$	5	15	45
2	$\langle\lambda_x\rangle^{\rm num}$, Eq. (55)	0.13 ± 0.01	0.27 ± 0.01	0.46 ± 0.01
3	$\langle\lambda_x\rangle^{\rm mod}$, Eq. (60)	0.13	0.26	0.48
4	$\mathcal{D}_{\rm bot}^{\rm fit}$, Eq. (56)	19 ± 5	33 ± 5	46 ± 5
5	$\mathcal{D}_{\rm bot}^{\rm mod}$, Eq. (60)	13	26	48
6	$\mathcal{D}_{\rm bot}^{\rm mix}$, Eq. (57c)	13	27	48

TABLE I. The increments λ_x and the width $\mathcal{D}_{\rm bot}$ for three values of $\mathcal{D}_{\rm par}$. The quantities are listed in lines: (1): $\mathcal{D}_{\rm par}$ [cf. Eqs. (55)]; (2): Numerically found value of $\langle\lambda_x\rangle^{\rm st} = \langle\lambda_x\rangle^{\rm num}$, Eqs. (55); (3): $\langle\lambda_x\rangle^{\rm st} = \langle\lambda_x\rangle^{\rm mod}$, found from the exponential model Eq. (57c); (4): The approximate width $\mathcal{D}_{\rm bot}^{\rm fit}$ of exponential fit Eq. (56), shown in Fig. 5 by dashed lines. (5):$\mathcal{D}^{\rm mod}$; (6): $\mathcal{D}_{\rm b}^{\rm mix}$ – "mixed" value of $\mathcal{D}_{\rm bot}$ found by the model Eq. (57c) in which λ_0 is numerically found $\langle\lambda_x\rangle^{\rm num}$ shown in the line 2.

3. *Exponential model of the bottom quasiparticles distribution*

Based on the results of the numerical solution of Eq. (55a), we assume that the profile n_x has an exponential form (56) with some yet unknown value $\mathcal{D}_{\rm bot}$. Under this assumption, we have two free parameters, λ_0 and $\mathcal{D}_{\rm bot}$. To find them, we need two relations. The first relation between them comes from the rate equation for the number of bottom quasiparticles $N_{\rm bot} = \int_0^\infty n_x dx$. We integrate the stationary Eq. (55a) with n_x given by Eq. (56) and take into account that the term Int_x vanishes upon integration. Then we have:

$$\frac{dN_{\rm bot}}{dt} = \langle\lambda_x\rangle\, N_{\rm bot}\,, \tag{57a}$$

$$\langle\lambda_x\rangle \equiv \int\limits_0^\infty \lambda_x n_x\, dx = \lambda_0 - \frac{\mathcal{D}_{\rm bot}}{x_0}\,. \tag{57b}$$

Obviously, Eq. (57a) describes a steady state if $\langle\lambda_x\rangle = 0$, i.e.

$$\mathcal{D}_{\rm bot} = x_0\,\lambda_0\,. \tag{57c}$$

The second relation between $\lambda_{\rm par}$ and $\mathcal{D}_{\rm bot}$ is provided by the first moment of Eq. (55a). Multiplying this equation by x and integrating over x from zero to infinity, we find:

$$0 = \langle x\,\lambda_x\rangle + \langle x\,\mathrm{Int}_x\rangle\,, \tag{58a}$$

$$\langle x\,\lambda_x\rangle = \int\limits_0^\infty x\lambda_x n_x\, dx = -x_0\lambda_0^2 = -\frac{\mathcal{D}_{\rm bot}^2}{x_0}\,. \tag{58b}$$

To simplifyn Eq. (58b) we used Eq. (57c).

With n_x given by Eq. (56), the integral (55a) for Int_x can be found analytically:

$$\begin{aligned}\mathrm{Int}_x =& n_x\Big[1+\mathrm{erf}\Big(\frac{x}{\sqrt{2}\mathcal{D}_{\rm par}}\Big)\\ &-\exp\Big(\frac{\mathcal{D}_{\rm par}^2}{2\mathcal{D}_{\rm bot}^2}\Big)\mathrm{erfc}\Big(\frac{\mathcal{D}_{\rm par}^2-\mathcal{D}_{\rm bot}x}{\sqrt{2}\mathcal{D}_{\rm bot}\mathcal{D}_{\rm par}}\Big)\Big]\,.\end{aligned} \tag{59}$$

Here, $\mathrm{erf}(z) = \frac{2}{\sqrt{\pi}}\int_0^z \exp(-t^2)dt$ is the Gauss error function and $\mathrm{erfc}(z) = 1-\mathrm{erf}(z)$.

Unfortunately, we cannot find the integral $\langle x\mathrm{Int}_x\rangle = \int\limits_0^\infty x\mathrm{Int}_x dx$ analytically. Therefore, we have solved Eqs. (58) for $\mathcal{D}_{\rm bot}$,

$$\begin{aligned}\mathcal{D}_{\rm bot}^2 =& x_0\int\limits_0^\infty x\, n_x\Big[1+\mathrm{erf}\Big(\frac{x}{\sqrt{2}\mathcal{D}_{\rm par}}\Big)\\ &-\exp\Big(\frac{\mathcal{D}_{\rm par}^2}{2\mathcal{D}_{\rm bot}^2}\Big)\mathrm{erfc}\Big(\frac{\mathcal{D}_{\rm par}^2-\mathcal{D}_{\rm bot}x}{\sqrt{2}\mathcal{D}_{\rm bot}\mathcal{D}_{\rm par}}\Big)\Big]dx,\end{aligned} \tag{60}$$

numerically. The results for $\mathcal{D}_{\rm bot}$ denoted $\mathcal{D}_{\rm bot}^{\rm mod}$ with $x_0 = 100$ (blue line) and $x_0 = 300$ (red line) are shown in Fig. 6b.

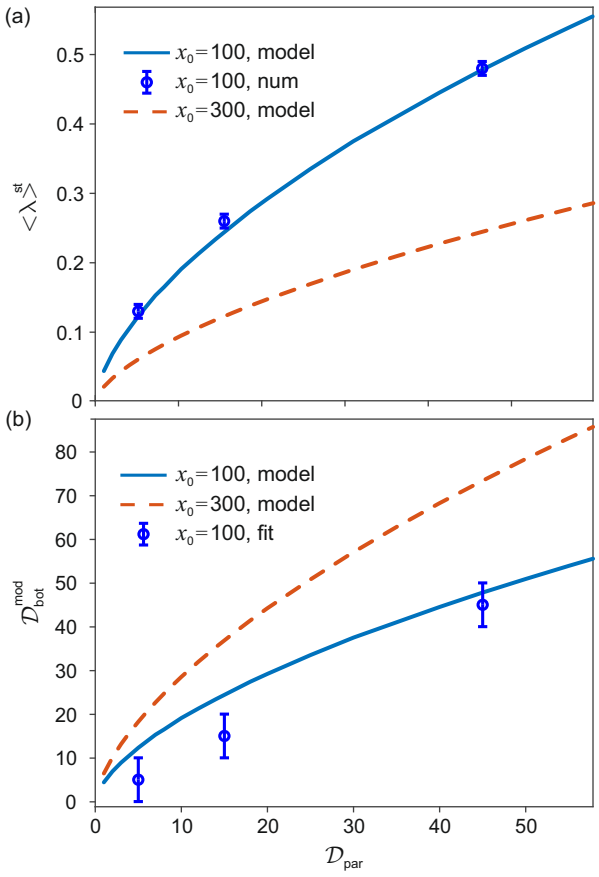

FIG. 6. Stationary solutions of the exponential model for (a) $\langle\lambda_x\rangle = \langle\lambda_x\rangle^{\rm st}$ [Eq. (57b)], and (b) $\mathcal{D}_{\rm bot}^{\rm mod}$, as a function of $\mathcal{D}_{\rm par}$. The results for $x_0 = 100$ are shown by solid blue lines and for $x_0 = 300$ by dashed red lines. Blue dots with error bars denote numerical values $\langle\lambda_x\rangle^{\rm st} = \langle\lambda_x\rangle^{\rm num}$ [Eq. (55b)] for $x_0 = 100$.

4. *Comparison of the numerical solution of quasiparticle rate equation and predictions of the exponential model*

To clarify how the solution of Eq. (60), derived in the framework of the approximations of the exponential model for the bottom quasiparticle distributions, corresponds to the "exact" numerical solution of the basic Eqs. (55), we compare corresponding results for the effective increment $\langle\lambda_x\rangle$, the characteristic width $\mathcal{D}_{\rm bot}$ and the effective increment λ_0 obtained in both ways.

a. Effective increment $\langle\lambda_x\rangle$. The values of $\langle\lambda_x\rangle^{\rm st} = \langle\lambda_x\rangle^{\rm num}$, found from numerical stationary solution of Eqs. (55), are given in line 2 of Tab. I. Corresponding values of $\langle\lambda_x\rangle^{\rm mod}$, obtained from the exponential model Eq. (57c) in which $\mathcal{D}_{\rm bot}^{\rm mod}$ is the solution of the model Eq. (60), are listed in line 3. To get a more general view on the model dependence $\langle\lambda_x\rangle$ vs $\mathcal{D}_{\rm par}$, we have presented these dependencies in Fig. 6(a) for $x_0 = 100$, blue line, and $x_0 = 300$, red line. Blue dots with error bars denote values of $\langle\lambda_x\rangle^{\rm num}$ found numerically for $x_0 = 100$, $\mathcal{D}_{\rm par} = 5$, 15 and $\mathcal{D}_{\rm par} = 45$. We see a very good quan-

titative agreement between these two approaches.

b. Effective width $\mathcal{D}_{\rm bot}$ in the approximate exponential distribution (56). The numerical profiles, shown by the solid lines in Fig. 5, where fitted by the exponential function (56) by finding the parameter $\mathcal{D}_{\rm bot}$ which minimizes the mean-square deviation. The resulting values of $\mathcal{D}_{\rm bot} = \mathcal{D}_{\rm bot}^{\rm fit}$ are given by line 4 in Tab. I, and the corresponding exponential profiles are shown in Fig. 5 by dashed lines. We see that although the fitted profiles describe the "exact" numerical profiles reasonably well, there are some systematic deviations between them. For example, for $\mathcal{D}_{\rm par} = 45$, the fitted profile goes above the numerical one for $n_x > 0.35$ while for $n_x < 0.35$, the fitted profile goes slightly below the numerical profile. This means that for $n_x > 0.35$ the current value of $\mathcal{D}_{\rm bot} < \mathcal{D}_{\rm bot}^{\rm fit} = 46$, while for $n_x < 0.35$ the current value of $\mathcal{D}_{\rm bot} > \mathcal{D}_{\rm bot}^{\rm fit} = 46$. Analyzing the current values of $\mathcal{D}_{\rm bot}$ for different x, we estimate the error bars as ± 5. For completeness, in line 6 of Tab. I we also list a "mixed" value of $\mathcal{D}_{\rm bot} = \mathcal{D}_{\rm bot}^{\rm mix}$ obtained from the model Eq. (57c) in which $\lambda_0 = \lambda_0^{\rm num}$. To complete the comparison, in Fig. 6, we have plotted the "fit" values of $\mathcal{D}_{\rm bot} = \mathcal{D}_{\rm bot}^{\rm fit}$ (blue dots with error bars), where the model dependence $\mathcal{D}_{\rm bot}$ vs. $\mathcal{D}_{\rm par}$ is shown for the same value of $x_0 = 100$ by the solid blue line.

In all the cases, we see a very reasonable agreement between the model values of $\langle \lambda_x \rangle$ and $\mathcal{D}_{\rm par}$ with the corresponding "exact" values found from the numerical solutions of the basic Eqs. (55).

As we have discussed above, the scattering of the bottom quasiparticles on the parametric ones results only in replacing of ν_0 by $\langle \nu_\omega \rangle$ in the rate Eq. (52) for $N_{\rm bot}$. In dimensionless units we need to replace λ_0, given Eq. (55b), by $\langle \lambda_x \rangle$, given in our exponential model by Eq. (57b):

$$\langle \lambda_x \rangle = \left(\frac{N_{\rm par}}{N_{\rm par}^{\rm cr}} \right)^2 - 1 - \frac{\mathcal{D}_{\rm bot}}{x_0} \,. \tag{61}$$

As before, the stationarity of the bottom quasiparticles requires $\langle \lambda_x \rangle = 0$, which can be achieved in the presence of scattering for some $N_{\rm par} \equiv N_{\rm par}^{\rm st} > N_{\rm par}^{\rm cr}$. Denoting the stationary value of $\langle \mu_x \rangle$ as $\langle \mu_x \rangle^{\rm st}$, we can write

$$\langle \mu_x \rangle^{\rm st} = \left(\frac{N_{\rm par}^{\rm st}}{N_{\rm par}^{\rm cr}} \right)^2 - 1 - \frac{\mathcal{D}_{\rm bot}}{x_0} = 0 \,, \tag{62}$$

or

$$N_{\rm par}^{\rm st} = N_{\rm par}^{\rm cr} \sqrt{1 + \mathcal{D}_{\rm bot}/x_0} \,. \tag{63}$$

Now, in order to account for the scattering of the bottom quasiparticles, we need to replace $N_{\rm p}^{\rm cr}$ by $N_{\rm par}^{\rm st} > N_{\rm par}^{\rm cr}$ in Eqs. (45b) and (45d) for the dependence of $N_{\rm par}$ and $N_{\rm bot}$ on hV. Considering for concreteness the case $\mathcal{D}_{\rm par} = 15$, we find $\lambda_0^{\rm mod} = 0.26$; see Tab. I. In Fig. 4 (solid lines), we have plotted the total number of the parametric $N_{\rm par}$ and the bottom quasiparticles $N_{\rm bot}$ vs. amplitude of the parametric pumping hV taking for concreteness $h^{\rm cr} = 10\gamma_{\rm par}$.

We see that for large enough hV the number of the bottom magnons can essentially exceed the number of the parametric magnons. In this case, besides the scattering of the bottom magnons on the parametric ones, one should also account for the four-magnon scattering in the subsystem of the bottom magnons and for the Kolmogorov-Zakharov cascade of the top magnons down to the bottom ones. The corresponding theory is beyond the scope of the present paper.

VI. EXPERIMENTAL RESULTS, DISCUSSION AND COMPARISON WITH THEORY

In the preceding sections, we discussed possible regimes of Bose-Einstein condensation for various intensities of the energy input. In Sec. III, we studied the BEC scenario under weak pumping, when quasiparticles (e.g., magnons) near the bottom of their frequency spectrum are in local thermodynamic equilibrium. In the following Sec. IV, we addressed Bose-Einstein condensation in the case of strong pumping, when quasiparticles are transferred from the pumping region to the BEC region at the bottom of the frequency spectrum by a step-by-step cascading Kolmogorov-Zakharov process. Section V was focused on the situation of ultra-strong pumping, in which there is a direct transfer of the pumped magnons to the spectrum bottom due to the process of kinetic instability. In particular, in Sec. V D, we developed a nonlinear theory of the kinetic instability that allowed us to find the frequency distribution of the bottom magnons and to estimate the number of magnons in both the pump and BEC regions as a function of pumping power.

The kinetic instability regime considered in Sec. V appears to be the most interesting from both theoretical and practical points of view. Being the physically most nontrivial regime, it also allows the formation of the densest magnon condensates suitable for practical applications. Therefore, in this Sec. VI, devoted to the experimental results, we focus on the case of ultra-strong parametric pumping of magnons. Here, we will compare our theoretical conclusions with both existing and new experimental data obtained in our work. Our main goal is to determine the main factors contributing to the transition of magnons toward the lower part of their frequency spectrum in YIG films and to analyze their frequency distribution in the BEC region.

A. Actual frequency spectrum in YIG films

Most experimental studies of the magnon Bose-Einstein condensation, as in this work, have been carried out in tangentially magnetized YIG films using parametric pumping and Brillouin light scattering (BLS) spectroscopy. This is because microwave parametric pumping is one of the most efficient methods of magnon injection, and BLS spectroscopy allows access to the broad

frequency–wave-vector domain of the magnon spectrum. The strong reduction of the BLS signal upon transition to normal magnetization of a magnetic film favors the use of tangential magnetization geometry. The low-damping ferrimagnetic YIG films provide the highest possible ratio between the spin-lattice relaxation time of the magnon gas and the thermalization time of the pumped magnons, which motivates the preference of these films over metallic ferromagnetic films or Heusler compounds.

To start our analysis of the experiment, we performed numerical calculations of the magnon frequency spectrum corresponding to our experimental conditions, i.e., in a 5.6-μm-thick YIG film tangentially magnetized by the magnetic field $H = 1500\,\mathrm{Oe}$ (see Fig. 7). This spectrum qualitatively corresponds to the spectra of all magnetic films with thicknesses ranging from a few microns to tens of microns, widely used in experimental studies of kinetic instability and Bose-Einstein condensation of magnons. In an unbounded film, the spectrum of magnon modes is discrete in the direction z normal to the film plane and continuous in its plane. Magnons condense at the lowest-frequency (fundamental) mode with the homogeneous or quasi-homogeneous distribution of dynamical magnetization over the film thickness. This mode $\omega(k_\parallel, k_\perp, k_z = 0)$ is shown in Fig. 7.

Unlike the spectrum presented in Fig. 1, the spectrum of magnons in tangentially magnetized films is strongly anisotropic, being very different for $\boldsymbol{k} = \boldsymbol{k}_\parallel \parallel \boldsymbol{H}$ (lower part of the spectrum, magenta curves), and for $\boldsymbol{k} = \boldsymbol{k}_\perp \perp \boldsymbol{H}$ (upper part, magenta curves). Gray curves show several intermediate directions of in-plane wave vectors $\boldsymbol{k} = (k_\parallel, k_\perp, k_z = 0)$. It is remarkable that for $\boldsymbol{k}_\parallel \parallel \boldsymbol{H}$ the spectrum has two equivalent minima with $k_\parallel = \pm k_{\mathrm{bot}}$ (with $k_{\mathrm{bot}} \approx 4.5 \cdot 10^4\,\mathrm{cm}^{-1}$). The red dots indicate the positions of these frequency minima $\omega_{\mathrm{bot}}(+\boldsymbol{q}_{\mathrm{bot}})$ and $\omega_{\mathrm{bot}}(-\boldsymbol{k}_{\mathrm{bot}})$ occupied by $+k$- and $-k$-BECs of magnons.

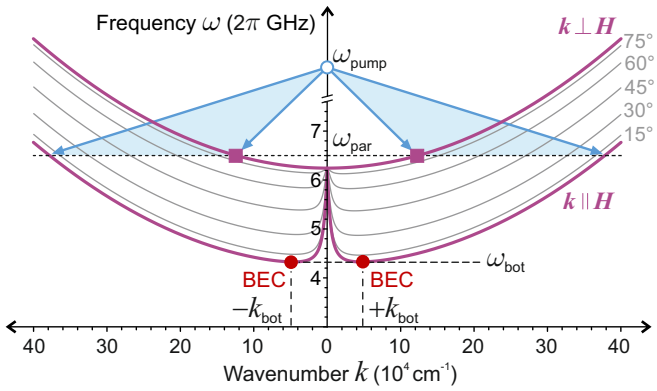

FIG. 7. The spectrum of the fundamental magnon mode in a 5.6-μm-thick YIG film planarly magnetized by a magnetic field $H = 1500\,\mathrm{Oe}$. The spectrum is shown for the wave vector $\boldsymbol{k} \parallel \boldsymbol{H}$, for $\boldsymbol{k} \perp \boldsymbol{H}$, and for several intermediate wave vector directions (gray curves). The blue arrows and light blue shadow areas illustrate the process of magnon injection by parallel parametric pumping with frequency ω_{pump}. The frequency of parametric magnons $\omega_{\mathrm{par}} = \omega_{\mathrm{pump}}/2$ is marked with a dotted line. The red dots indicate the positions of the frequency minima $\omega_{\mathrm{bot}}(+\boldsymbol{k}_{\mathrm{bot}})$ and $\omega_{\mathrm{bot}}(-\boldsymbol{k}_{\mathrm{bot}})$ occupied by $+k$- and $-k$-BECs of magnons. The two magenta squares show the magnon pair with the lowest threshold of parametric instability [43].

Blue arrows and light blue shadow areas illustrate the process of magnon injection by parallel parametric pumping leading to filling by parametric magnons the entire surface $\omega(\boldsymbol{k}) = \omega_{\mathrm{pump}}/2$ for large pumping power [32].

Despite the significant difference between the spectra presented in Fig. 1 and Fig. 7, the qualitative results obtained in the previous sections remain valid. Both cases can be described by the same Gross-Pitaevskii equations with the position of the frequency minima properly rescaled, as well as the scale of wave vectors in their vicinity. The theory developed for the isotropic dispersion law (1a) can be easily generalized to the case of the real spectrum of a YIG film shown in Fig. 7. The main reason is that the processes of BE condensation occur in each frequency minimum independently and practically identically, as is confirmed by our experiments. The number of quasiparticles near each minimum is approximately equal, $N^+_{\mathrm{tot}} \approx N^-_{\mathrm{tot}}$ and each of them (and not only their sum) is an integral of motion. [44].

For example, in the quasi-equilibrium regime under weak pumping, discussed in Sec. III, one should replace the simple Eqs. (11a) and (12) for $E^{\mathrm{3D}}_{\mathrm{tot}}$ and $N^{\mathrm{3D}}_{\mathrm{gas}}$ obtained for the isotropic dispersion law (1a) with a sum of two contributions, obtained near each minimum of the "realistic in YIG" frequency spectra. In this case, we do not have an equally simple expression, and the integration should be performed numerically for the actual frequency spectrum. However, the qualitative result that BEC occurs only if the wavenumber localization of the quasiparticle influx k_{f} is below some critical value k_{cr}, which is independent of the value of f, still holds. Similarly, in the case of strong pumping, we cannot obtain analytical results in the $k \sim \pm k_0$ regions for the values and direction of the energy and number of particle fluxes for the "realistic in YIG" dispersion law. Nevertheless, for large enough $k \gg k_0$, when the exchange interaction dominates, the quadratic dispersion law (1a) is recovered, and our results from Sec. (IV) are valid directly. In this case, the particle flux goes down to the region of small k and then separates into two equal fluxes going to each minimum separately. Most of our theoretical results for the case of ultra-strong pumping are not sensitive to the particular form of the dispersion law and, as we will see below, can be directly compared with experiments.

B. Experimental procedure

The experiments were performed using samples with a YIG film of a thickness 5.6 μm and 6.7 μm. All samples were grown by liquid-phase epitaxy in (111) crystallo-

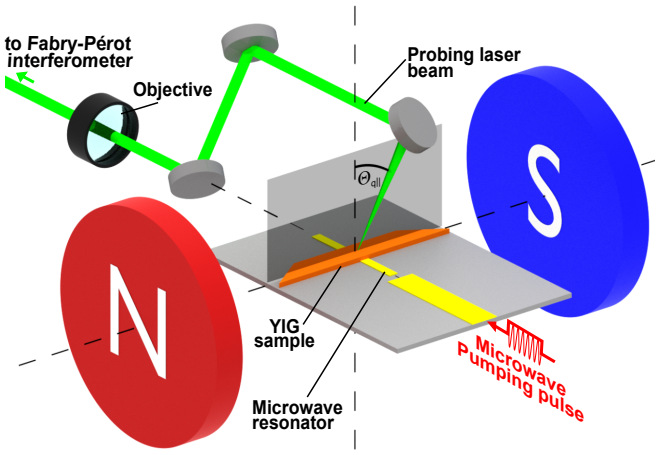

FIG. 8. Schematic setup of the wave-vector-resolved BLS experiment. The probing laser beam is focused on the parametrically pumped area of the YIG sample by an objective lens. The laser light incidence angle $\Theta_{q\parallel}$ is steered using a combination of three dielectric mirrors mounted on a rotary stage (not shown), allowing for a change in the incident angle from $-90°$ to $90°$. The plane of incidence is oriented along the direction of the bias magnetic field. Therefore, the probed magnon wave vectors are also oriented in the same direction. Light inelastically scattered by magnons propagates along the backward path and is directed using a beam splitter (not shown) to the Fabry-Pérot interferometer for frequency analysis and photon counting.

graphic plane on a gallium gadolinium garnet substrate.

To detect the magnons, we used Brillouin light scattering spectroscopy that allowed us to obtain the frequency-, wave-vector-, space-, and time-resolved spectra. It was equipped with electromagnetic parametric pumping circuits.

The experimental setup is shown schematically in Fig. 8. To achieve a large amplitude of the pumping magnetic field and, thus, a high magnon density, microwave pumping is supplied using half-wavelength microstrip resonators with a quality factor of about 25. The samples were placed in the middle of the resonators in the antinode of the microwave magnetic field. Both 50 µm- and 100 µm-wide microstrip resonators, with resonance frequencies of 13.2 GHz, 13.6 GHz, and 14.4 GHz were utilized. The pumping was performed with 1 µs long pulses with the peak power of up to 40 W. A repetition interval of more than 200 µs ensured that the spin system is brought into equilibrium and that the thermal stability of the sample is maintained from pulse to pulse. The bias magnetic field $\boldsymbol{H}$ was oriented perpendicular to the longitudinal axis of the resonators in the plane of the samples.

A probing laser beam of 532 nm wavelength is focused onto a spot with a diameter of about 20 µm in the parametrically pumped area of the YIG films. By setting the beam incidence angle $\Theta_{k\parallel}$ in a plane perpendicular to the film surface and oriented along the $\boldsymbol{H}$ bias field (see Fig. 8), one can selectively detect magnons with wave vectors $\boldsymbol{k}_\parallel$ [45]. Varying $\Theta_{k\parallel}$ from 0 to $\pm 58°$ allows us to detect magnons with wave vectors ranging from 0 to $\pm 2 \cdot 10^5\,\mathrm{cm}^{-1}$ with a resolution of about $1.5 \cdot 10^3\,\mathrm{cm}^{-1}$ [46].

In the backward Brillouin scattering geometry used, the component of the wave vector of the probing light lying in the film plane is reversed due to interaction with magnons. The component perpendicular to the film plane reverses direction by elastic reflection [43]. Thus, it is necessary to ensure efficient and spatially homogeneous reflection of the probing beam after it passes through the film. This is achieved by covering the surface of the 6.7 µm-thick films facing the pump resonator with a thin dielectric mirror coating (< 1 µm) [45–47]. In the experiments with 5.6 µm-thick YIG films, light reflection occurred from the surface of the microstrip pumping resonator, which was in direct contact with the YIG film [43, 48]. The scattered light is sent to the Fabry-Pérot interferometer to analyze the Stokes and anti-Stokes spectral components, whose frequency shifts are equal to the magnon frequencies and whose intensities are proportional to the corresponding magnon densities.

A temporal analysis of the magnon dynamics with a resolution of up to 400 ps is achieved by recording the moments of detection of the scattered photons relative to the moment of application of the pump pulse [46, 49]. The spatial analysis is realized by moving the sample together with the pump resonator relative to the BLS measurement point [46, 49].

The automation system thaTEC:OS (THATec Innovation GmbH) [50] was used to control the experimental setup and to collect data.

C. Spatial distribution of bottom magnons at various magnetic fields

Before proceeding to the experimental verification of the obtained theoretical results, we need to clearly define the region of experimental parameters at which one of the two mechanisms of the transition of parametric magnons to the bottom of the frequency spectrum prevails: the Kolmogorov-Zakharov cascade described in Sec. IV and the kinetic instability of bottom magnons analyzed in Sec. V. For this purpose, we started with studying the spatial distribution of the bottom magnons in the pumping area at different magnetic fields H.

In these measurements, we employed a 100 µm-wide microstrip pumping resonator and a 6.7 µm-thick YIG film. The dielectric mirror coating of this sample allowed us to make measurements not only directly above the resonator but also in the surrounding regions of the YIG film. Owing to this mirror coating, the intensity of the back-scattered light is independent of the reflectivity of the microstrip material and its dielectric substrate and thus reflects the magnon density distribution well. The pumping frequency, determined by the length

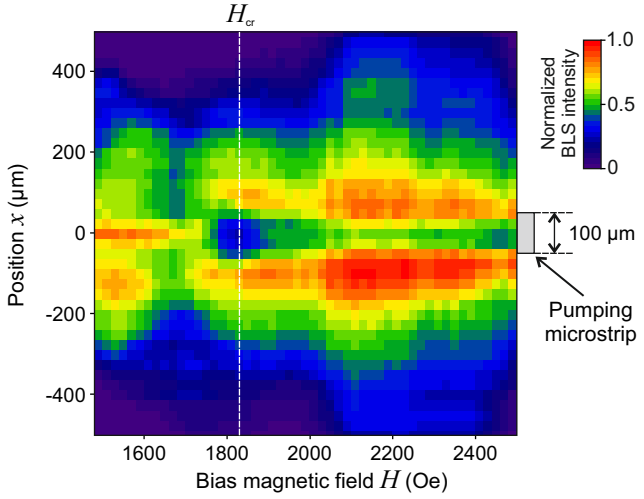

FIG. 9. Spatial distribution of the bottom magnon density across a 100 μm-wide microstrip pumping resonator measured for different magnetizing fields H. The pumping frequency is 14.4 GHz.

of the microstrip resonator, was 14.4 GHz. The maximum available pumping power in our experiment was applied, which was 40 W.

The incident angle $\Theta_{k\|}$ was set to 11°, which corresponded to the detection of magnons with wave numbers around $4.5 \cdot 10^4$ cm^{-1}. Therefore, only magnons from the bottom part of the spectrum (see Fig. 7) were registered. The spatial distribution of the BLS intensity plotted in Fig. 9 consists of the integrated anti-Stokes parts of two different spectra of inelastically scattered light measured for angles $\Theta_{k\|} = \pm 11°$. Thus, the $\pm k$ bottom magnons are shown simultaneously in this figure.

At the longitudinal axis of the resonator, where the microwave pumping magnetic field is parallel to the bias field H, the conditions for the parallel pumping [51, 52] are realized. At the edges of the resonator, where the pump field is perpendicular to the field H, perpendicular pumping occurs [51, 52]. In the latter case, the direct pumping source is not the external electromagnetic field itself but the dynamic magnetization non-resonantly driven by this field.

At a field $H = H_{\rm cr}$, corresponding to the minimal threshold of parametric instability, a blue region of low concentration of near-bottom magnons is well visible above the resonator. In this case, under the conditions of parallel pumping, parametric magnons with relatively small wave vectors $\boldsymbol{k}_\perp \perp \boldsymbol{H}$ and a frequency close to the ferromagnetic resonance frequency are excited, as schematically shown in Fig. 7 by the two magenta squares. For this magnon group, the process of kinetic instability is forbidden by the laws of conservation of energy and momentum [22, 35]. The BLS intensity increases for lower and higher magnetic fields since the kinetic instability process allowed here leads to a higher magnon density at the bottom of the spectrum.

At the same time, for perpendicular pumping, when magnons with large wave vectors directed at an angle of 45–55° to $\boldsymbol{H}$ are excited [51], there is no such strict prohibition. Consequently, no such significant difference in the bottom magnon density is observed at the sides of the microstrip resonator over the entire range of the bias magnetic fields. Moreover, the magnons excited by perpendicular parametric pumping propagate at non-zero angles to the resonator axis over quite considerable distances, thus expanding the spatial region of the overpopulated magnon gas. As a result, the area populated by bottom magnons born from the kinetic instability process is also expanded.

The conducted measurements allow us to determine the regions of the film in which the physical mechanisms of injection, thermalization, and spectral transfer of magnons analyzed in the previous sections are realized in the best and simplest way. Based on our findings, we can distinguish regions with parallel and perpendicular pumping of parametric magnons. Going forward, we will concentrate on the most effective and well-researched case of parallel pumping. In doing so, we avoid the need to take into account the spatial transport of parametric magnons and the associated effective damping.

D. From kinetic instability to BEC

In the previous section, we observed a distinct forbidden area, surrounded by two regions of the allowed kinetic instability at lower and higher magnetic fields. To delve deeper into this phenomenon and to reveal the connection between the processes of kinetic instability and Bose-Einstein condensation, we have conducted an extensive experimental analysis of its properties under parallel parametric pumping.

To increase the amplitude of the pumping magnetic field, we used a resonator of 50 μm width. The BLS measurements were carried out in the 5.6 μm-thick film at a point on the longitudinal axis of this resonator, i.e., under the exclusive action of parallel pumping. The pumping frequency of 13.6 GHz was determined by the resonator geometry. The obtained results are presented in Fig. 10.

An analysis of the conservation laws in thin YIG films performed in Ref. [35] for the same experimental conditions as in the current work shows that the kinetic instability is allowed in two ranges of magnetic field: Area 1 – from $H_{1,\rm min} \approx 1100$ Oe to $H_{1,\rm max} \approx 1600$ Oe; and Area 2 – from $H_{2,\rm min} \approx 1750$ Oe to $H_{2,\rm max} \approx 2400$ Oe.

In Figure Fig. 10(a), the blue empty circles show the dependence of the parametric instability threshold $h_{\rm th}$, introduced by Eq. (45e), on the magnetic field. We see that in area 1, below $H_{\rm cr} = 1700$ Oe, the value of $h_{\rm th}$ is practically independent of H. Bearing in mind that with good accuracy $\omega_0 \propto H$ and that the wave vectors of the parametric magnons $\boldsymbol{k}_{\rm par}$ satisfy the relation $\omega_{\boldsymbol{k}_{\rm par}} = \omega_{\rm pump}/2$ decreasing to zero when H approaching $H_{\rm cr}$, we conclude that in this area the damping of para-

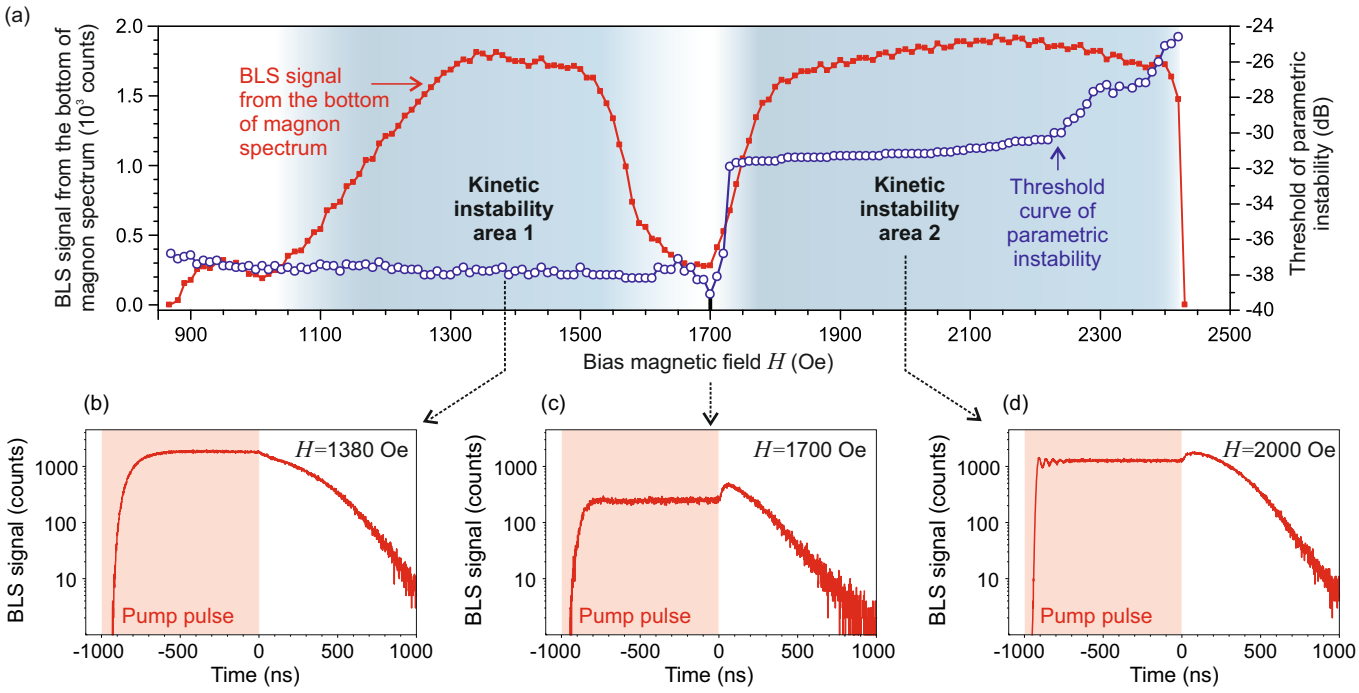

FIG. 10. Panel (a): Measured parametric instability threshold (red squares) compared to the BLS signal from the bottom of the magnon spectrum (blue empty circles). Areas with blue shading, in which KI processes are allowed by the momentum and energy conservation laws, are marked as the "Kinetic instability area 1 and 2". Panels (b), (c), and (d) show the temporal dynamics of BLS signals from bottom magnons in the presence [panels (b) and (d)] and absence [panel (c)] of the kinetic instability process. The pumping frequency is 13.6 GHz.

metric magnons $\gamma_{\boldsymbol{k}} \propto h_{\rm th}$ is practically independent of $\boldsymbol{k}$. For many reasons not discussed here, the relationship between $\gamma_{\boldsymbol{k}}$ and $h_{\rm th}$ in area 2 is more complicated [51], and here we leave the question about k-dependence of $\gamma_{\boldsymbol{k}}$ for $H > H_{\rm cr}$ open.

In the same Fig. 10(a), we also show by red squares the magnetic field dependence of the BLS signal intensity proportional to the total number of bottom magnons. It can be seen that in areas free from the kinetic instability, the number of the BLS counts is about 250, while with the KI active it jumps up to about 1800. As seen from the comparison with Fig. 9, this dependence correlates well with the density of bottom magnons on the magnetic field measured on the longitudinal axis of a wide (100 µm) pumping resonator. The difference in the value of the critical field $H_{\rm cr}$ in Fig. 9 and Fig. 10(a) is due to the difference in the frequencies of parametric pumping. We interpret these observations as evidence that the dominant contribution to the bottom magnons (above 80%) comes from the kinetic instability and only a small part (below 20%) originates from the cascade processes.

The temporal dynamics of BLS signals from the bottom magnons are shown in the presence [see Figs. 10(b,d)] and absence [see Figs. 10(c)] of the kinetic instability process. In the latter case, one finds a significantly lower density of the bottom magnons during the pumping action and a jump-like increase in their density after turning off. This jump is the result of the effective population of the lowest energy states by the Kolmogorov-Zakharov scattering cascade after the pumping field is turned off and the disappearance of frequency-localized dense groups of parametric magnons.

A similar but smaller jump in the magnon density can be seen in panel (d). In this case, the parametric magnons are excited closer to the bottom of the spectrum, and the Kolmogorov-Zakharov cascade plays a role comparable to the kinetic instability process.

Concluding, we have to stress that when we compare our theoretical results with experimental findings, we must keep in mind that the pure impact of either the Kolmogorov-Zakharov cascade or the kinetic instability on particle transfer down to the BEC region is not fully realized. Instead, what we typically observe is a combination of these two mechanisms.

E. Frequency–wave-number distribution of magnons

In the sections VI C and VI D, we presented qualitative arguments in favor of the important role of the kinetic instability process in transporting parametrically injected magnons to the lower end of their frequency spectrum. In this section, we share our experimental data on the frequency–wave-vector magnon distribution

under microwave pumping. The analysis of this distribution reveals several specific nonlinear processes, including the four-wave scattering process (32) responsible for the kinetic instability. This gives us greater confidence that we are dealing with the kinetic instability phenomenon in our experiments, allowing us to compare it with our theory given in Sec. V.

Figure 11 shows the BLS intensity spectra $I(\omega, k_\parallel)$ of magnons with wave vectors $\boldsymbol{k} = \boldsymbol{k}_\parallel \parallel \boldsymbol{H}$. $I(\omega, k_\parallel)$ is proportional to the density of the corresponding magnons $n(\omega, k_\parallel)$. The spectra $I(\omega, k_\parallel)$ were measured during microwave pumping at 13.2 GHz in a YIG film magnetized in plane by the field $H = 1885$ Oe. The solid red line shows the calculated magnon frequency spectrum $\omega_{k_\parallel}$, which has two minima $\omega_{\rm bot} \equiv \min_{k_\parallel}\{\omega_{k_\parallel}\} \approx 4\cdot(2\pi)$ GHz at $k_\parallel = \pm k_{\rm bot}$ with $k_{\rm bot} \approx 4\cdot 10^3\,{\rm cm}^{-1}$. The two brightest spots in the vicinity of the bottom of the magnon spectra $\omega_{\rm bot}$, $\pm k_{\rm bot}$ originate from the "bottom" magnons associated with the left and right BEC states. They are spread around the bottom of the spectrum due to the scattering of the bottom magnons on the parametric ones $\omega(\boldsymbol{k}_{\rm bot}+\boldsymbol{\kappa}_1)+\omega(\boldsymbol{k}_{\rm par}+\boldsymbol{\kappa}_2) = \omega(\boldsymbol{k}_{\rm bot}+\boldsymbol{\kappa}_3)+\omega(\boldsymbol{k}_{\rm par}+\boldsymbol{\kappa}_4)$, which was discussed in Sec. V. Here, $\boldsymbol{\kappa}_1+\boldsymbol{\kappa}_2 = \boldsymbol{\kappa}_3+\boldsymbol{\kappa}_4$ and $\kappa_j \ll k_{\rm bot}$.

Above these brightest spots we see three spots with $\omega \approx 2\omega_{\rm bot}$ and $k_{\rm left} \approx -2k_{\rm bot}$, $k_{\rm center} \approx 0$, and $k_{\rm right} \approx 2k_{\rm bot}$. They are related to the confluence of two bottom magnons, as shown by green arrows in Fig. 11(a):

i) left spot, $\omega_{-k_\parallel}+\omega_{-k_\parallel} \Rightarrow 2\omega_{\rm bot}$ and $k = -2k_{\rm bot}$;

ii) central spot, $\omega_{-k_\parallel}+\omega_{+k_\parallel} \Rightarrow 2\omega_{\rm bot}$ and $k = 0$;

iii) right spot, $\omega_{+k_\parallel}+\omega_{+k_\parallel} \Rightarrow 2\omega_{\rm bot}$ and $k = 2k_{\rm bot}$.

Note that neither $\omega = 2\omega_{\rm bot}$ with $k = \pm 2k_{\rm bot}$ nor $\omega = 2\omega_{\rm bot}$ with $k = 0$ are eigenmodes of the YIG film in our magnetization geometry. Therefore, what we see are the off-resonant waves driven by an appropriate nonlinearity, i.e., virtual magnons, called "double-bottom virtual magnons" in [53].

In Fig. 11(a), the BLS spectra $I(\omega, k_\parallel)$ are supplemented by two down-pointing orange arrows showing the process of parametric pumping by the external quasi-homogeneous microwave field with wave vector $\boldsymbol{k}_{\rm pump} \approx 0$ and frequency $\omega_{\rm pump}$. Precisely at this position, we see a rather bright spot, indicating virtual "pumped" magnons [53]. At the same time, at the frequency of the parametrically pumped real magnons $\omega_{\rm par} = \omega_{\rm pump}/2$ we see no BLS response because the wave numbers of the parametric magnons are pretty large and lie outside the sensitivity range of our BLS setup.

Two more spots visible at $\omega_{\rm top} = 2\omega_{\rm par} - \omega_{\rm bot}$ and $k_{\rm top} = \pm k_{\rm bot}$ indicate magnons with frequency of the top magnons involved in the kinetic instability process [see Eq. (32)].

If so, then the top magnons must have wave vectors $\boldsymbol{k}_{\rm top} = \boldsymbol{k}_1 + \boldsymbol{k}_2 \mp \boldsymbol{k}_{\rm bot}$, where $\boldsymbol{k}_1$ and $\boldsymbol{k}_2$ are the wave vectors of the parametric magnons with $\omega(\boldsymbol{k}_1) = \omega(\boldsymbol{k}_2) = \omega_{\rm pump}/2$. Assuming for a rough estimate that $\omega_{\rm top} > \omega_{\rm bot}$, we conclude that $k_{\rm top} \gtrsim k_1$ and $k_{\rm top} \gtrsim k_2$, meaning that the top magnons lie outside the sensitivity region of our BLS setup, i.e., they are invisible in Fig. 11. The origin of the two spots in Fig. 11(b) at frequency $\omega_{\rm top} = \omega_{\rm pump} - \omega_{\rm bot}$, which is consistent with Eq. (32), but with wave vectors $\boldsymbol{k}_{\rm top} = \pm\boldsymbol{k}_{\rm bot}$ was clarified in [53]. It was stressed that the theory of kinetic instability is formulated in the framework of the weak-wave kinetic equation, which assumes weak correlations of the wave phases. As a result, the scattering (43c) of real magnons has a stochastic nature and appears only as the second-order perturbation of the four-wave interaction

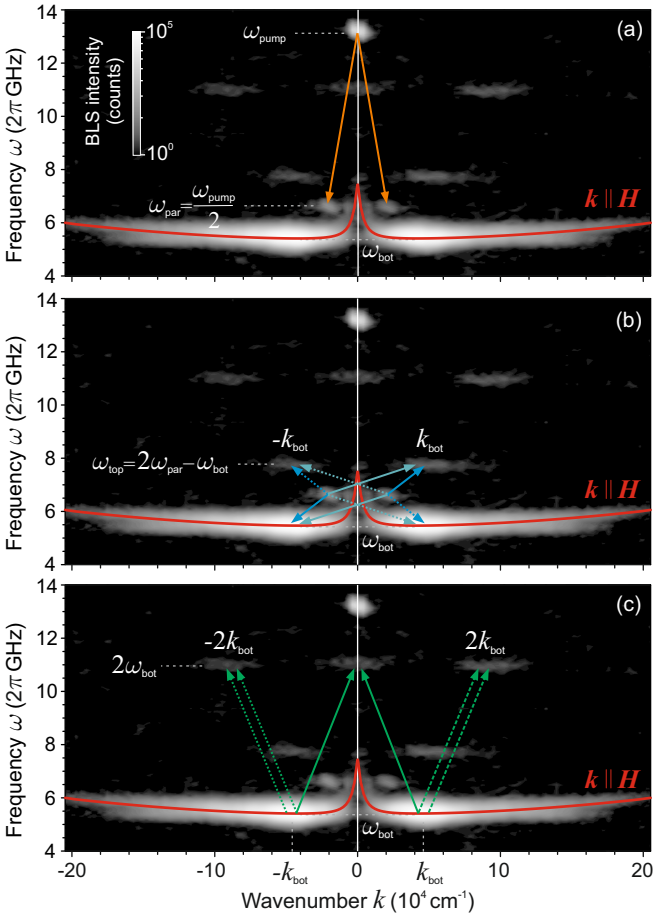

FIG. 11. Frequency- and wave-vector-resolved BLS intensity spectrum of real and virtual magnons. The spectra were measured during the action of 13.2 GHz microwave pumping on a YIG film magnetized in plane by the field $H = 1885$ Oe. The BLS intensity is proportional to the magnon density. The experimental intensity spectrum is shown together with the calculated magnon dispersion curve and diagrams showing the relevant quasiparticle scattering processes in the system: (a) Orange arrows show the process of parametric pumping. The signal of virtual "pump" magnons is visible at the pumping frequency $\omega_{\rm pump}$. (b) The four-magnon kinetic instability processes leading to the appearance of virtual "top" magnons at $\omega_{\rm top}$ frequency are shown by pairs of solid and dashed blue and cyan arrows. (c) Virtual "double-bottom" magnons at the frequency $2\omega_{\rm bot}$ arise due to the confluence of the bottom magnons at $\omega_{\rm bot}$. Upward green arrows show the relevant confluence processes.

amplitudes $W^{\mathbf{3,4}}_{\mathbf{1,2}}$, Eq. (24b). Nevertheless, in our particular case with a large population of parametric and bottom magnons, there are strong, externally determined, phase correlations of the scattering waves. In particular, the full phase correlation in the pairs of parametric waves with $\pm\boldsymbol{k}_{\rm par}$ arises due to their interaction with the space-homogeneous pumping field [32]. Given this correlation, $|\langle a_{\boldsymbol{k}_{\rm par}} a_{-\boldsymbol{k}_{\rm par}} \exp[i\omega_{\rm par}]\rangle| = \langle |a_{\boldsymbol{k}_{\rm par}}|^2\rangle \equiv n_{\boldsymbol{k}_{\rm par}}$. This allows us to consider a pair of parametric magnons $(a_{\boldsymbol{k}_{\rm par}} a_{-\boldsymbol{k}_{\rm par}})$ as a "single", coherent wave object with the frequency $2\omega_{\rm par} = \omega_{\rm pump}$ and phase being the sum of the phases of the waves composing the pair. Therefore, four-wave scattering (43c) with $\boldsymbol{k}_1 = -\boldsymbol{k}_2$, $\boldsymbol{k}_3 = \pm\boldsymbol{k}_{\rm bot}$, due to its dynamic nature, appears much stronger than stochastic scattering with $\boldsymbol{k}_1 \neq -\boldsymbol{k}_2$, being now proportional to the first power of the interaction amplitude $W^{\mathbf{3,4}}_{\mathbf{1,2}}$, and producing the driving force [53]

$$F = \sum_{\boldsymbol{k}_{\rm par}} T^{\boldsymbol{k}_{\rm par},-\boldsymbol{k}_{\rm par}}_{\pm\boldsymbol{k}_{\rm bot},\mp\boldsymbol{k}_{\rm bot}} a^*_{\mathbf{2}} a_{\boldsymbol{k}_{\rm par}} a_{-\boldsymbol{k}_{\rm par}} \ . \tag{64}$$

This force has the same frequency (32) as that of real top magnons [see Eq. (61)] but with the different wave vector $\boldsymbol{q}_{\rm top} = \mp\boldsymbol{q}_{\rm bot}$. This force excites off-resonant magnons, seen in two bright spots, as discussed earlier.

F. Pumping power dependence of the parametric and bottom magnon numbers

In Fig. 4, we plot theoretical predictions for the dependence of the total number of parametric and bottom magnons, $N_{\rm par}$ and $N_{\rm bot}$ as a function of the relative amplitude of the microwave pumping field $\dfrac{hV}{\gamma_{\rm par}} = \dfrac{h}{h_{\rm th}}$. Our theory considers only the kinetic instability mechanism of the transfer of parametric magnons to the lower magnon region and does not take into account the mechanism of the step-by-step Kolmogorov-Zakharov cascade. Therefore, for the comparison of theory and experiment, we have to choose the range of bias magnetic fields H, where kinetic instability is allowed, see Fig. 10. In the range of lower magnetic fields H, denoted "kinetic instability area 1", the wave numbers of the parametric magnons are large and cannot be detected by BLS spectroscopy. For this reason, we have chosen for the comparison the magnetic field range designated as "kinetic instability area 2", taking for the sake of concreteness $H = 1885$ Oe as in Fig. 11.

In Fig. 12, one can see the numbers of BLS counts $\mathcal{N}_{\rm par}$ and $\mathcal{N}_{\rm bot}$ obtained from the parametric and bottom magnons at different pumping supercriticalities $h/h_{\rm th}$ and represented by blue circles and red squares, respectively. Assuming a smooth dependence of $\mathcal{N}_{\rm par}$ and $\mathcal{N}_{\rm bot}$ on $h/h_{\rm th}$, we used the procedure of interpolating the experimental data by a cubic spline, which resulted in the blue and red solid lines. Moreover, we used the available data to extrapolate the desired dependence of $\mathcal{N}_{\rm par}$ and $\mathcal{N}_{\rm bot}$ on $h/h_{\rm th}$ to the region of low pumping powers, where the low signal-to-noise ratio did not allow for experimental observations. These results are shown by blue and red dashed lines. By finding the value of h, at which $\mathcal{N}_{\rm par} \to 0$, we accurately estimated the threshold value $h_{\rm th}$ for parametric instability. This value was used to normalize the scale of the abscissa axis in Fig. 12. Since the sensitivity of the BLS setup to parametric and bottom magnons is different, the ratio $\mathcal{N}_{\rm par}/\mathcal{N}_{\rm bot}$ does not reflect the ratio of their occupation numbers $N_{\rm par}/N_{\rm bot}$. However, these experimental curves correctly reproduce the dependence of $N_{\rm par}$ and $N_{\rm bot}$ on h in units of the threshold field of parametric instability.

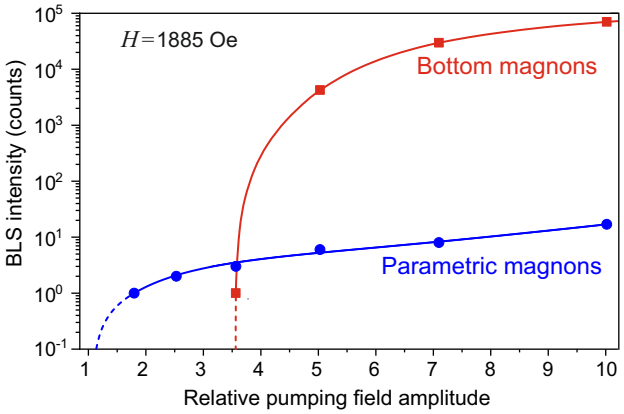

FIG. 12. Dependence of the number of BLS counts from the parametric magnons $\mathcal{N}_{\rm par}$ (blue circles) and that from the bottom magnons $\mathcal{N}_{\rm bot}$ (red squares) on the pumping field amplitude h normalized by the parametric instability threshold $h_{\rm th}$. $H = 1885$ Oe. The pumping frequency is 13.2 GHz. The solid red and blue curves represent an interpolation and an extrapolation of the corresponding experimental data using cubic splines. The dashed lines are extrapolations of the experimental dependencies in the region of relatively low levels of parametric pumping.

A comparison of the theoretically predicted dependencies of $N_{\rm par}$ and $N_{\rm bot}$ on $h/h_{\rm th}$ shown in Fig. 4 with the experimental results shown in Fig. 12 demonstrates a fairly good qualitative agreement. This is a strong argument for the validity of our nonlinear theory of kinetic instability, which evidences that this theory captures the essential physical mechanisms governing the phenomenon.

At the same time, the experimental data shown in Fig. 12 does not demonstrate a pronounced saturation of the dependence $N_{\rm par}(h/h_{\rm th})$, as predicted by the theory. This may be due to some secondary effects, such as the relatively small contribution of the Kolmogorov-Zakharov cascade to the particle flux towards lower frequencies, which is not yet considered in our theory. Another possible origin of the discrepancy is a change in the magnon excitation region caused by a downward frequency shift of the magnon spectrum due to a decrease in magnetization at high pumping powers and a consequent increase in the efficiency of parametric pumping.

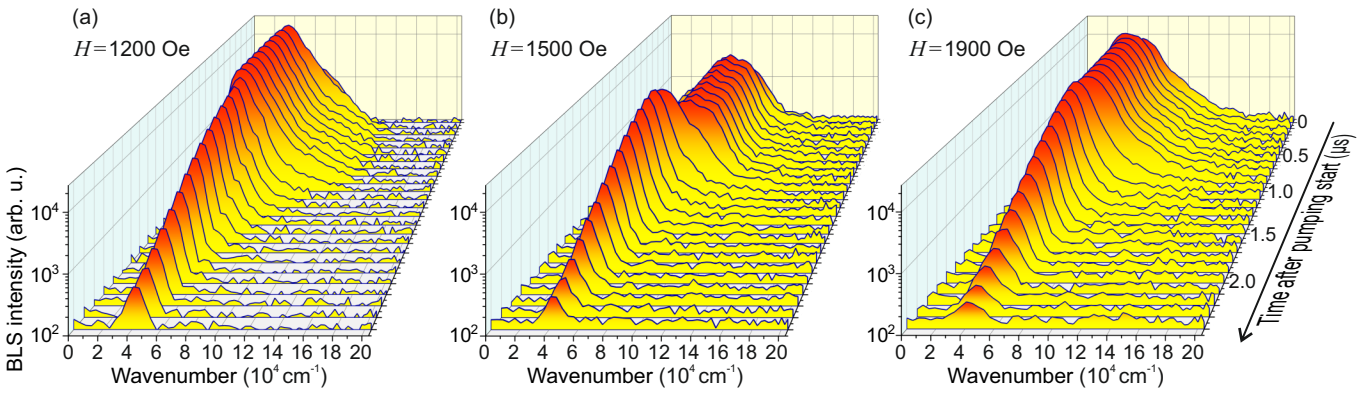

FIG. 13. Distributions of the bottom magnons by wave numbers at different time delays after pumping was turned on. Panels (a), (b), and (c) show three-dimensional plots for three different bias magnetic fields H. The pumping pulse has a duration of 1 μs (note the direction of the time axis). To improve the signal-to-noise ratio, we integrated the spectra in the time window of 100 ns and over the entire frequency range of the bottom magnons. The pumping frequency is 13.2 GHz.

G. Time evolution at different magnetic fields

In Sections VI C, VI D, and VI E, we theoretically analyzed different aspects of the behavior of bottom magnons during parametric pumping. We concluded that the kinetic instability essentially contributes to the transfer of magnons to their frequency minimum. In addition, the nonlinear kinetic instability theory developed in Sect. V D also accounts for the scattering of the bottom magnons on the parametric magnons and shows that this scattering leads to a broadening of the near-bottom magnon distribution in the vicinity of $\boldsymbol{k}_{\rm bot}$, $\omega_{\rm bot}$. If this scattering ceases, we expect bottom magnons to evolve into BECs, narrowing their frequency and wave vector spectra.

Fortunately, the theory of kinetic instability suggests how to test this statement experimentally: one can study the evolution of the distribution of the near-bottom magnons over frequencies and wave vectors after turning off the parametric pumping. The frequency of parametric magnons is higher than that of the bottom magnons. Therefore, we can expect that their relaxation $\gamma_{\rm par}$ in the linear regime is larger than the linear relaxation $\gamma_{\rm bot}$ of the bottom magnons. When the number of parametric magnons is very large, the kinetic instability opens a very efficient additional dissipation channel for parametric magnons. This means that even if, in the linear regime, the relaxation rates of parametric and bottom magnons are approximately equal, in the nonlinear regime, the relaxation rate of parametric magnons is much larger than that of the bottom magnons. Consequently, after pumping is turned off, there is a period during which parametric magnons are practically absent, while bottom magnons continue to exist, and the expected narrowing of their spectrum can be detected.

According to Ref. [54], the distribution of magnons in a system has been significantly narrowed down, as measured by detecting electromagnetic radiation in the frequency domain. The resolution of BLS spectroscopy is not fine enough to record this effect, but we have a good resolution in the wave-number domain, as shown in Fig. 11. By integrating the frequency distribution of the bottom magnons, in Fig. 13 we plotted the BLS intensity versus the magnon wave number $k_\parallel$ and time for different magnetic fields after turning on the parametric pumping.

Examining the data, we can see that during the first 1 μs of the pumping pulse, the peak of the distribution of bottom magnons in $\boldsymbol{k}$-space has a relatively constant and broad shape. However, after the pumping is switched off, this peak quickly narrows, which aligns with our theoretical expectations. Eventually, the peak width reaches the limit of the wave number resolution.

Figure 13(a) with $H = 1200$ Oe corresponds to region 1 of the kinetic instability, see Fig. 10, while Fig. 13(c) with $H = 1900$ Oe corresponds to region 2 of the kinetic instability. In these cases, the parametric magnons are transferred directly to the bottom of the spectrum.

In Fig. 13(b), where $H = 1500$ Oe, the Kolmogorov-Zakharov cascade plays an important role in the magnon distribution process. This results in a significant portion of magnons being distributed between the parametric and the bottom parts of the $\boldsymbol{k}$-space. When the pumping is switched off, these magnons continue to move towards the bottom, creating an intense hump that is clearly visible in Fig. 10(b).

Another perspective on the BLS spectra is shown in Fig. 14. We now integrated them over wave number, obtaining frequency spectra for different magnetic fields and times after switching off the parametric pumping. In panel (a) we plot the results for the small magnetic field $H = 1200$ Oe. The value of $\omega_{\rm bot}/(2\pi) \approx 3.5$ GHz is shown as a vertical black dashed line, while $2\omega_{\rm bot}/(2\pi)$ is shown as a vertical black dotted line. One sees an intense peak of the bottom magnons and a much smaller peak (by about three orders of magnitude) of the double-bottom virtual magnons. The parametric magnons with the frequency $\omega_{\rm par} = \omega_{\rm pump}/2$, shown by the vertical red dotted line, are not seen in this panel. They have large wave num-

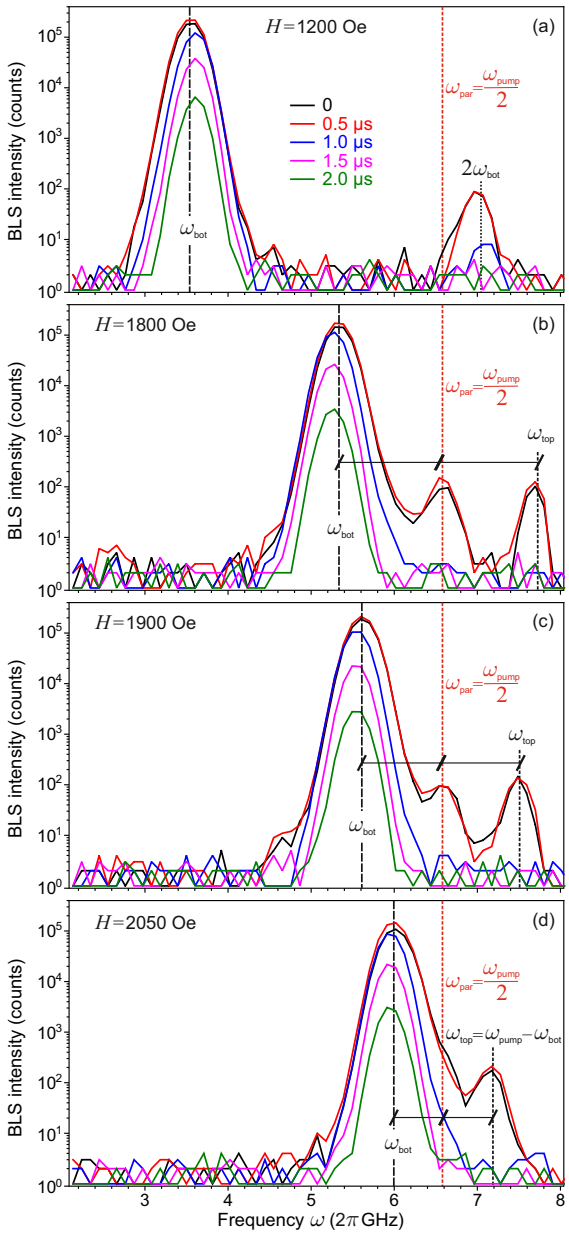

FIG. 14. Frequency spectra at varios bias magnetic fields and varios times after pumping is switched off. The pumping frequency is 13.2 GHz.

bers that are outside of the accesible zone for our BLS setting. For a larger magnetic field, the wave numbers decrease and we see peaks of the parametric magnons in Figs. 14(b,c). For the largest magnetic field $H = 2050$ Oe, shown in Fig. 14(d), the frequency of the parametric magnons is very close to the very intense peak of the bottom magnons. Therefore the peak of the parametric magnons just slightly disturbs the peak of the bottom magnons.

In all Figs. 14(b)-14(d) for $H > 1200$ Oe, the frequency $2\omega_{\rm bot}$ is outside the accesible zone and the peak $2\omega_{\rm bot}$ seen in Fig. 14(a) has disappeared. Instead, we see a peak at $\omega_{\rm top}$ that is exactly at the required position $\omega_{\rm pump} - \omega_{\rm bot}$. This is another confirmation that the kinetic instability essentially contributes to the population of the bottom magnons.

As an additional support for the kinetic instability picture, we note the absence of a continuous magnon distribution between $\omega_{\rm par}$ and $\omega_{\rm bot}$, expected in the case of the Kolmogorov-Zakharov step-by-step cascade.

In summary, the experimental findings and discussions presented in this section lead us to conclude that the primary cause of the transfer of magnons from the region of their parametric pumping with the frequency of $\omega_{\rm par} = \omega_{\rm pump}/2$ to the bottom of their frequency spectrum $\omega_{\rm bot}$ is the kinetic instability discussed in Sec. V. The experiments confirm that the main mechanism that limits the number of bottom magnons is their feedback effect on the parametric magnons, as described in Section Sec. V B. Additionally, the experiments confirm that the scattering of the bottom magnons on parametric ones, described in Sec. V D, plays the leading role in widening the bottom magnons' distributions.

VII. SUMMARY

We presented a systematic and comprehensive description of the physical mechanisms leading to the Bose-Einstein condensation of quasiparticles. Unlike the atomic BEC forming in the thermodynamic equilibrium conditions, the quasiparticles condense under conditions of flux equilibrium and represent a nonlinear wave system with energy pumping and dissipation. We find the conditions under which Bose-Einstein condensation of quasiparticles is possible. The first and obvious constraint that we took into account is the conservation (or almost complete conservation) of the total number of quasiparticles in the non-linear processes. This means that the four-wave scattering processes $2 \Leftrightarrow 2$ must dominate over the three-wave processes near the bottom of the frequency spectrum.

We started in Sec. III, with the pumping weak enough to keep the wave system close to the thermodynamic equilibrium. In this case, it is necessary to simply balance the pumping and damping rates of the total number of quasiparticles $N_{\rm tot}$ and the total energy in the system, giving the conditions under which the total number $N_{\rm tot}$ of quasiparticles in the system exceeds the number of quasiparticles $N_{\rm gas}$. The excess $N_{\rm BEC} = N_{\rm tot} - N_{\rm gas}$ can occupy excited energy levels and create a BE-condensate at the zero energy level.

The situation with strong pumping is less straightforward. It is necessary to consider the kinetic wave equation to describe the transport of quasiparticles from the pumping range to the lower part of the wave frequency spectrum. In Sec. IV, we have done this under the assumption of the scale invariance of the system. In this case, analytic solutions of the kinetic equation are available. For the $2 \Leftrightarrow 2$ scattering, the kinetic equation can have two differently oriented solutions for the energy and

particle fluxes. We have specified the conditions under which the particle flux is oriented toward small k, allowing the creation of a BE-condensate.

An even more complicated scenario is realized by a super-strong injection of quasiparticles into a narrow frequency range, for example, by high-power parametric pumping. In this case, the relaxation rate of quasiparticles becomes negative, first at small wave vectors k at the lower part of the frequency spectrum. This leads to the phenomenon of exponential growth of the number of quasiparticles with small k, known as kinetic instability. In Sec. V, we developed a nonlinear theory of kinetic instability that considers the feedback of unstable bottom quasiparticles on their source – the parametrically excited quasiparticles. This theory also accounts for the $2 \Leftrightarrow 2$ scattering of bottom quasiparticles on parametric quasiparticles, which broadens the bottom quasiparticle packet.

In the last section Sec. VI, we presented an experimental study of BE magnon condensation in yttrium iron garnet thin films using Brillouin light scattering spectroscopy. The theoretical and experimental results are in qualitative agreement. Therefore, we conclude that, if allowed by conservation laws, the kinetic instability serves as the dominant source of bottom magnons in the vicinity of their BE-condensation points, and that the nonlinear theory of kinetic instability developed in V describes the main physical mechanisms of this process quite well. The above comparison of our analytical findings and experimental observations opens new directions for further studies of this phenomenon.

ACKNOWLEDGEMENTS

This study was funded by the Deutsche Forschungsgemeinschaft (DFG, German Research Foundation) – TRR 173 – 268565370 Spin+X (Project B04). D.A.B. acknowledges support by grant ECCS-2138236 from the National Science Foundation of the United States. V.S.L. was partly supported by NSF-BSF grant # 2020765.

[1] A. D. Stone, *Einstein and the Quantum: The Quest of the Valiant Swabian* (Princeton University Press, 2015).
[2] A. Einstein, Quantentheorie des einatomigen idealen Gases. Zweite Abhandlung (German) [Quantum theory of the monatomic ideal gas. Second Treatise], in *Albert Einstein: Akademie-Vorträge, Sitzungsberichte der Preußischen Akademie der Wissenschaften 1914–1932*, edited by D. Simon (Wiley-VCH Verlag, 2005) pp. 245–257.
[3] Bose, Plancks Gesetz und Lichtquantenhypothese, Z. Phys. **26**, 178 (1924).
[4] H. Fröhlich, Bose condensation of strongly excited longitudinal electric modes, Phys. Lett. A **26**, 402 (1968).
[5] D. Snoke, Coherent questions, Nature **443**, 402 (1978).
[6] K. B. Davis, M.-O. Mewes, M. R. Andrews, N. J. van Druten, D. S. Durfee, D. M. Kurn, and W. Ketterle, Bose–Einstein condensation in a gas of sodium atoms, Phys. Rev. Lett. **75**, 3969 (1995).
[7] M. H. Anderson, J. R. Ensher, M. R. Matthews, C. E. Wieman, and E. A. Cirnell, Observation of Bose–Einstein condensation in a dilute atomic vapor, Science **269**, 3969 (1995).
[8] A. Amo, J. Lefrère, S. Pigeon, C. Adrados, C. Ciuti, I. Carusotto, R. Houdré, E. Giacobino, and A. Bramati, Superfluidity of polaritons in semiconductor microcavities, Nat. Phys. **5**, 805 (2009).
[9] J. P. Eisenstein and A. H. MacDonald, Bose–Einstein condensation of excitons in bilayer electron systems, Nature **432**, 691 (2004).
[10] J. Klaers, J. Schmitt, F. Vewinger, and M. Weitz, Bose–Einstein condensation of photons in an optical microcavity, Nature **468**, 545 (2010).
[11] Y. M. Bunkov and G. E. Volovik, Bose–Einstein condensation of magnons in superfluid 3He, J. Low Temp. Phys. **150**, 135 (2007).
[12] S. O. Demokritov, V. E. Demidov, O. Dzyapko, G. A. Melkov, A. A. Serga, B. Hillebrands, and A. N. Slavin, Bose–Einstein condensation of quasi-equilibrium magnons at room temperature under pumping, Nature **443**, 430 (2006).
[13] A. A. Serga, V. S. Tiberkevich, C. W. Sandweg, V. I. Vasyuchka, D. A. Bozhko, A. V. Chumak, T. Neumann, B. Obry, G. A. Melkov, A. N. Slavin, and B. Hillebrands, Bose–Einstein condensation in an ultra-hot gas of pumped magnons, Nat. Commun. **5**, 3452 (2014).
[14] M. Schneider, T. Brächer, D. Breitbach, V. Lauer, P. Pirro, D. A. Bozhko, H. Y. Musiienko-Shmarova, B. Heinz, Q. Wang, T. Meyer, F. Heussner, S. Keller, E. T. Papaioannou, B. Lägel, T. Löber, C. Dubs, A. N. Slavin, V. S. Tiberkevich, A. A. Serga, B. Hillebrands, and A. V. Chumak, Bose–Einstein condensation of quasiparticles by rapid cooling, Nat. Nanotechnol. **15**, 457 (2020).
[15] P. Türschmann, H. L. Jeannic, S. F. Simonsen, H. R. Haakha, S. Götzinger, V. Sandoghdar, P. Lodahl, and R. Nir, Coherent nonlinear optics of quantum emitters in nanophotonic waveguides, Nanophotonics **10**, 1641 (2019).
[16] M. Fukami, D. R. Candido, D. D. Awschalom, and M. E. Flatté, Opportunities for long-range magnon-mediated entanglement of spin qubits via on- and off-resonant coupling, PRX Quantum **2**, 040314 (2021).
[17] C. Lai, N. Y. Kim, S. Utsunomiya, G. Roumpos, H. Deng, M. D. Fraser, T. Byrnes, P. Recher, N. Kumada, T. Fujisawa, and Y. Yamamoto, Coherent zero-state and π-state in an exciton-polariton condensate array, Nature **450**, 529 (2007).
[18] V. V. Zautkin, B. I. Orel, and V. B. Cherepanov, Parametric excitation of spin waves by noise modulation of their frequencies, Sov. Phys. JETP **58**, 414 (1983).
[19] Y. D. Kalafati and V. L. Safonov, Theory of quasiequilibrium effects in a system of magnons excited by incoherent pumping, Sov. Phys. JETP **73**, 836 (1991).

[20] A. V. Chumak, G. A. Melkov, V. E. Demidov, O. Dzyapko, V. L. Safonov, and S. O. Demokritov, Bose–Einstein condensation of magnons under incoherent pumping, Phys. Rev. Lett. **102**, 187205 (2009).

[21] A. Lavrinenko, V. S. L'vov, G. A. Melkov, and V. B. Cherepanov, "Kinetic" instability of a strongly nonequilibrium system of spin waves and tunable radiation of a ferrite, Sov. Phys. JETP **54**, 542 (1981).

[22] G. A. Melkov and S. V. Sholom, Kinetic instability of spin waves in thin ferrite films, Sov. Phys. JETP **72**, 341 (1991).

[23] G. Melkov, V. Safonov, A. Taranenko, and S. Sholom, Kinetic instability and bose condensation of nonequilibrium magnons, J. Magn. Magn. Mater. **132**, 180 (1994).

[24] F. London, The λ-point of liquid helium and the Bose–Einstein degeneracy, Nature **141**, 643 (1938).

[25] Y. M. Kagan, B. V. Svistunov, and S. G. V., Kinetics of Bose condensation in an interacting Bose gas, Sov. Phys. JETP **74**, 279 (1992).

[26] D. A. Bozhko, A. A. Serga, P. Clausen, V. I. Vasyuchka, F. Heussner, G. A. Melkov, A. Pomyalov, V. S. L'vov, and B. Hillebrands, Supercurrent in a room-temperature Bose–Einstein magnon condensate, Nat. Phys. **12**, 1057 (2016).

[27] S. Nazarenko, *Wave Turbulence*, Lecture Notes in Physics, Vol. 825 (Springer-Verlag, 2011).

[28] L. D. Landau and E. M. Lifshitz, *Statistical Physics*, 3rd ed., Course of Theoretical Physics, Vol. 5 (Butterworth Heinemann, 1980).

[29] V. E. Zakharov, V. S. L'vov, and G. Falkovich, *Kolmogorov Spectra of Turbulence I. Wave Turbulence*, Springer Series in Nonlinear Dynamics (Springer-Verlag, 1992).

[30] L. D. Landau and E. M. Lifshitz, *Quantum Mechanics: Non-Relativistic Theory*, 3rd ed., Course of Theoretical Physics, Vol. 3 (Pergamon Press, 1977).

[31] R. Fjørtoft, On the changes in the spectral distribution of kinetic energy for twodimensional, nondivergent flow, Tellus **5**, 225 (1953).

[32] V. S. L'vov, *Wave Turbulence Under Parametric Excitation. Applications to Magnets*, Springer Series in Nonlinear Dynamics (Springer-Verlag, 1994).

[33] S. Dyachenko, A. C. Newell, A. Pushkarev, and V. E. Zakharov, Optical turbulence: weak turbulence, condensates and collapsing filaments in the nonlinear Schrödinger equation, Physica D **57**, 96 (1992).

[34] J. Skipp, V. L'vov, and S. Nazarenko, Wave turbulence in self-gravitating Bose gases and nonlocal nonlinear optics, Phys. Rev. A **102**, 043318 (2020).

[35] A. J. E. Kreil, D. A. Bozhko, H. Y. Musiienko-Shmarova, V. I. Vasyuchka, V. S. L'vov, A. Pomyalov, B. Hillebrands, and A. A. Serga, From kinetic instability to Bose–Einstein condensation and magnon supercurrents, Phys. Rev. Lett. **121**, 077203 (2018).

[36] V. S. L'vov and V. Cherepanov, Nonlinear theory of the "kinetic" excitation of waves, Sov. Phys. JETP **54**, 746 (1981).

[37] B. V. Semisalov, V. N. Grebenev, S. B. Medvedev, and S. V. Nazarenko, Numerical analysis of a self-similar turbulent flow in Bose–Einstein condensates, Commun. Nonlinear Sci. Numer. Simul. **102**, 105903 (2021).

[38] H. Suhl, Note on the saturation of the main resonance in ferromagnetics, J. Appl. Phys. **30**, 1961 (1959).

[39] E. Schlömann, Longitudinal susceptibility of ferromagnets in strong rf fields, J. Appl. Phys. **33**, 527 (1962).

[40] V. Zakharov, V. S. L'vov, and S. Starobinets, Spin-wave turbulence beyond the parametric excitation threshold, Sov. Phys. Usp. **17**, 896 (1975).

[41] V. S. L'vov, *Nonlinear Spin Waves* (in Russian, Nauka, 1987).

[42] V. S. L'vov and G. E. Fal'kovich, On the interaction of parametrically excited spin waves with thermal spin waves, Sov. Phys. JETP **55**, 904 (1982).

[43] A. A. Serga, C. W. Sandweg, V. I. Vasyuchka, M. B. Jungfleisch, B. Hillebrands, A. Kreisel, P. Kopietz, and M. P. Kostylev, Brillouin light scattering spectroscopy of parametrically excited dipole-exchange magnons, Phys. Rev. B **86**, 134403 (2012).

[44] M. Mohseni, V. I. Vasyuchka, V. S. L'vov, A. A. Serga, and B. Hillebrands, Classical analog of qubit logic based on a magnon Bose–Einstein condensate, Commun. Phys. **5**, 196 (2022).

[45] D. A. Bozhko, H. Y. Musiienko-Shmarova, V. S. Tiberkevich, A. N. Slavin, I. I. Syvorotka, B. Hillebrands, and A. A. Serga, Unconventional spin currents in magnetic films, Phys. Rev. Res. **2**, 023324 (2020).

[46] P. Frey, D. A. Bozhko, V. S. L'vov, B. Hillebrands, and A. A. Serga, Double accumulation and anisotropic transport of magnetoelastic bosons in yttrium iron garnet films, Phys. Rev. B **104**, 014420 (2021).

[47] A. J. E. Kreil, H. Y. Musiienko-Shmarova, P. Frey, A. Pomyalov, V. S. L'vov, G. A. Melkov, A. A. Serga, and B. Hillebrands, Experimental observation of Josephson oscillations in a room-temperature Bose–Einstein magnon condensate, Phys. Rev. B **104**, 144414 (2021).

[48] D. A. Bozhko, A. J. E. Kreil, H. Y. Musiienko-Shmarova, A. A. Serga, A. Pomyalov, V. S. L'vov, and B. Hillebrands, Bogoliubov waves and distant transport of magnon condensate at room temperature, Nat. Commun. **10**, 2460 (2019).

[49] O. Büttner, M. Bauer, A. Rueff, S. Demokritov, B. Hillebrands, A. Slavin, M. Kostylev, and B. Kalinikos, Space- and time-resolved Brillouin light scattering from nonlinear spin-wave packets, Ultrasonics **38**, 443 (2000).

[50] Thatec innovation gmbh, `https://thatec-innovation.com/`, [Accessed: 26-August-2022].

[51] T. Neumann, A. A. Serga, V. I. Vasyuchka, and B. Hillebrands, Field-induced transition from parallel to perpendicular parametric pumping for a microstrip transducer, Appl. Phys. Lett. **94**, 192502 (2009).

[52] O. Dzyapko, V. E. Demidov, M. Buchmeier, T. Stockhoff, G. Schmitz, G. A. Melkov, and S. O. Demokritov, Excitation of two spatially separated Bose-Einstein condensates of magnons, Phys. Rev. B **80**, 60401(R) (2009).

[53] V. S. L'vov, A. Pomyalov, D. A. Bozhko, B. Hillebrands, and A. A. Serga, Correlation-enhanced interaction of a Bose–Einstein condensate with parametric magnon pairs and virtual magnons, Phys. Rev. Lett. **131**, 156705 (2023).

[54] T. B. Noack, V. I. Vasyuchka, A. Pomyalov, V. S. L'vov, A. A. Serga, and B. Hillebrands, Evolution of room-temperature magnon gas: Toward a coherent bose-einstein condensate, Phys. Rev. B **104**, L100410 (2021).